UNIVERSIDAD DE CHILE
FACULTAD DE CIENCIAS FÍSICAS Y MATEMÁTICAS
DEPARTAMENTO DE ASTRONOMÍA

STUDY OF THE CIRCUMGALACTIC ENVIRONMENT OF THE MERGER SYSTEM J205724.14 AT $z \sim 4.6$ USING ALMA

TESIS PARA OPTAR AL GRADO DE
MAGÍSTER EN CIENCIAS, MENCIÓN ASTRONOMÍA

MELISSA FRANCISCA FUENTEALBA FUENTES

PROFESORA GUÍA:
PAULINA LIRA TEILLERY

MIEMBROS DE LA COMISIÓN:
TANIO DIAZ SANTOS
RICARDO MUÑOZ VIDAL
MANUEL ARAVENA AGUIRRE

SANTIAGO DE CHILE
2023

ESTUDIO DEL MEDIO CIRCUNGALACTICO DEL MERGER J205724.14 A $z \sim 4.6$ USING ALMA

Comprender cómo evolucionan las galaxias a lo largo del tiempo es la clave para entender cómo crecieron estos sistemas a partir de pequeñas perturbaciones impresas en el fondo cósmico de microondas (CMB) hasta las galaxias observadas en el Universo local. Se espera que la conexión entre el agujero negro supermasivo (SMBH) que se encuentra en el centro de una galaxia y la galaxia anfitriona sea compleja, con indicios de crecimiento coevolutivo respaldado por evidencia observacional y por simulaciones. A alto-z, se sugiere que un SMBH y su galaxia anfitriona están siendo alimentados por un depósito común de gas como consecuencia de al menos dos procesos: la interacción cercana entre galaxias conocida como fusiones o la acumulación de gas frío desde el medio inter/circungaláctico (IGM/CGM). Ambos mecanismos aumentarían la formación de estrellas (SF) de la galaxia y la acreción eficiente del SMBH durante una fase de intensa actividad del núcleo galáctico activo (AGN). Para probar la contribución de estos procesos de forma observacional, debemos centrarnos en las primeras épocas de la evolución de las galaxias, donde debería tener lugar esta coevolución. Para lograr observaciones tan distantes, se requiere de tecnologías avanzadas como las disponibles con el Atacama Large Millimeter/submillimeter Array (ALMA).

En esta tesis, investigamos el estado dinámico de J205724.14, un sistema de fusión en curso compuesto por un cuásar (QSO) a $z \sim 4.6$ y una galaxia polvorienta compañera (DSFG) a una distancia espacial de ~ 20 kpc. Las fuentes fueron reportadas previamente por Nguyen et al. (2020) como parte de una muestra de doce objetos observados durante el ciclo 4 de ALMA. En este trabajo, presentamos el análisis de las observaciones del ciclo 6 de ALMA de la línea de emisión en el infrarrojo lejano (FIR) [CII], que surge del medio interestelar (ISM) de las galaxias y la emisión de continuo FIR subyacente que traza el polvo calentado por la actividad estelar.

A partir de este análisis, observamos dos componentes principales, el QSO y la DSFG, detectados en [CII] y en continuo, con múltiples blobs vecinos detectados solo en [CII]. Tres de estos blobs forman la cola de marea que se extiende desde el cuásar hacia el oeste en una dirección recta por ~ 10 kpc. Esta morfología perturbada respalda la hipótesis de un escenario de fusión. Además, se observa un desplazamiento de velocidad de aproximadamente -68 km s^{-1} entre el QSO y la DSFG que sugiere que realmente están experimentando una fuerte interacción gravitacional. Al ajustar un modelo de distribución de energía espectral (SED) a los datos del continuo, estimamos tasas de formación de estrellas (SFR) $\sim 402 \pm 51\ M_{\odot}$ año^{-1} para el QSO y $\sim 244 \pm 38\ M_{\odot}$ año^{-1} para la DSFG, ubicándolos sobre o cerca de la secuencia principal de galaxias (MS). Esto es particularmente interesante teniendo en cuenta que J205724.14 QSO fue seleccionado por ser uno de los cuásares no oscurecidos más brillantes a este redshift pero muestra una SFR bastante modesta. Basándose en el modelo evolutivo de cuásares de Sanders et al. (1988), se espera este resultado para un cuásar que ya ha pasado una fase oscurecida de rápida SF durante un proceso de fusión de galaxias. Sin embargo, vemos que el evento de fusión en nuestro sistema está lejos de haber terminado y debería encontrarse en algún lugar entre el primer pericentro y los posteriores pasajes cercanos. El trabajo futuro incluye publicar esta investigación y solicitar observaciones más profundas utilizando ALMA y JWST, lo que nos permitiría resolver la galaxia anfitriona y la DSFG y tener una medición adecuada de sus propiedades.

STUDY OF THE CIRCUMGALACTIC ENVIRONMENT OF THE MERGER SYSTEM J205724.14 AT $z \sim 4.6$ USING ALMA

Understanding how galaxies evolve through time is the key to understand how these systems grew from tiny perturbations imprinted in the cosmic microwave background (CMB) to the galaxies observed in the local Universe. The connection between the supermassive black hole (SMBH) found at the center of a galaxy and the host itself is expected to be complex, with hints of co-evolutionary growth which is supported by observational evidence as well as simulations. At high-z it is suggested that a SMBH and its host are being fueled by a common reservoir of gas as a consequence of at least two processes: the close interaction between galaxies known as mergers or the accretion of cold gas from the inter/circumgalactic medium (IGM/CGM). Both mechanisms would enhance the star formation (SF) of the galaxy and the efficient SMBH accretion during a phase of active galactic nuclei (AGN) activity. To test the contribution of these processes observationally, we need to focus at the early epochs of the evolution of galaxies, where this coevolution should be taking place. For such distant observations, advanced technologies such as those available with the Atacama Large Millimeter/submillimeter Array (ALMA) are required.

In this thesis, we investigate the dynamical state of J205724.14, an ongoing merger system composed by a quasar (QSO) at $z \sim 4.6$ and a companion dusty star-forming galaxy (DSFG) at a spatial distance of ~ 20 kpc. The sources were previously reported by Nguyen et al. (2020) as part of a sample of twelve targets observed during ALMA Cycle 4. In this work, we present the analysis of ALMA cycle 6 observations of the far-infrared (FIR) emission line [CII], which arises from the interstellar medium (ISM) of the galaxies and underlying FIR continuum emission that traces the dust heated by the starburst activity.

From this analysis, we observed two main components, the QSO and the DSFG, detected in [CII] and continuum emission and multiple neighbouring blobs detected only in [CII]. Three of these clumps form the tidal tail that extends from the quasar in a straight direction to the west for ~ 10 kpc. This perturbed morphology supports the hypothesis of a merging scenario. Additionally, a velocity offset of about -68 km s^{-1} is observed between the QSO and the DSFG suggesting that they are indeed experiencing a strong gravitational interaction. By fitting a spectral energy distribution (SED) model to the continuum data, we estimate star formation rates (SFRs) of $\sim 402 \pm 51$ $M_\odot$ yr^{-1} for the QSO host and $\sim 244 \pm 38$ $M_\odot$ yr^{-1} for the DSFG, which locate them on or close to the main sequence of star-forming galaxies (MS). This is particularly interesting considering that J205724.14 QSO was selected for being one of the brightest unobscured quasars at its redshift but it shows a rather modest SFR. Based on Sanders et al. (1988) evolutionary model of quasars, this result is expected for a quasar that has already passed an obscured phase of rapid SF during a major merger. However, we see that the merger event in our system is far from finished and it should be found somewhere between the first pericenter and subsequent close passages. Future work includes publishing this research and requesting deeper observations using ALMA and JWST which would allow us to resolve the QSO host and DSFG and have a proper measurement of their properties.

Para mi Vita, Francisca Hernández.

Agradecimientos

Le agradezco a mi mamá Eli Fuentes y a mi papá Víctor Fuentealba que me apoyaron en salir de Linares a estudiar a la gran ciudad. Lo dieron todo durante estos años para que yo pudiera estar aquí. A mi hermana pequeña Arantza que me da todo su amor y apoyo siempre, eres mi orgullo piojito. Los amo a los tres.

A mi mejor amiga Caterin, mi moritz, por escucharme y acompañarme en la distancia y a la Karina que me mandaba mensajitos diciendo que me extrañaba. A mi Jael (yeil) que fue mi mayor pilar en todo el plan común, no sé que habría sido de mí sin ti. A mi comarca, la Ale y Alexis, que pasaban todos los días conmigo en la salita y los domingos en la kinder, haciendo tareas, riendo y cantando, son lo más lindo. Al Silvio por apañar siempre en todo lo que le pidiera y al Alex por ser mi super senpai. A la gente de Calán, Paula y Priya por hacerme reir en nuestras reuniones de AGN y al Felipe que nunca me creía que yo iba a Calán los miércoles.

Quiero agradecer a todas las personas que me acompañaron en mi tesis, principalmente a mi profe, Paulina Lira, que me dió la oportunidad de trabajar con ella y en este proyecto en el que pude explorar lo que quería investigar, muchas gracias por el apoyo, la confianza y la empatía, sobretodo en los años de pandemia. También agradecerle a Tanio Díaz-Santos que me recibió en Grecia a pesar de que solo le había escrito unos cuantos correos y nada más, gracias por ayudarme cuando parecía que mis datos nunca iban a dejarme trabajarlos y por continuar guiándome con tanta paciencia durante todo el año pasado. A Manuel Aravena y Ricardo Muñoz, gracias por la buena disposición a formar parte de mi comisión y por sus comentarios con los que pude terminar (al fin!) esta tesis. Gracias a Ana Posses porque se ofreció durante mi primer año de magister a ayudarme con mis datos y por dejar que me uniera a sus reuniones con el profe Manuel y con Jorge. Gracias a Liza Videla que me guió con todas mis dudas de ALMA y a mi madre griega, Anna, prometo que nos veremos de nuevo.

Especialmente, le agradezco a Joaquín Lagos, mi pololo, por estar dispuesto a seguirme a cualquier rincón del mundo al que yo quisiera partir. Eres esa parte de mi vida que le da sentido a todo. Te amo más de lo que puedo explicar en estas líneas. Finalmente, gracias a la familia de Joaquín, que me dan mucho cariño y que me recibieron en su casa todo este tiempo para que pudiera terminar esta tesis acá en Santiago.

Table of Content

List of Tables

List of Figures

Chapter 1

Introduction

The Universe is organized into different levels of structures with galaxies being considered one of the large scale building blocks. Indeed, galaxies are complex systems formed by stars, gas, dust, and dark matter, which are all joined together by gravity. Even though they all tend to be dragged by the large scale structure of the universe and located in groups or clusters (nodes in the cosmic web), galaxies come in a vast range of shapes and colors. Due to their different morphologies and properties, the classification of galaxies has a long history of trying to find the proper categories to organize them and therefore inferring their paths of formation and evolution, which are the key to understanding the evolution of the Universe as a whole.

In recent years, not only galaxies but their circumgalactic medium (CGM) has become a pivotal component for deciphering how all these structures evolve. The CGM is defined as the gas located outside the disks or interstellar medium (ISM) of the galaxies and inside their virial radius[1]. The CGM is a complex, mostly diffuse medium composed of multiphase gas, which means that the gas exists in different volumes with species at different ionization potentials that allow us to derive a diversity of physical conditions, such as temperature and density. The gas in the CGM can be found as highly ionized gas (when T $> 10^6$ K), moderately ionized gas (T $\sim 10^4$ K) and neutral gas (T $\sim 10^2$ K) (Tumlinson et al., 2017).

To our advantage, we can access not only the Universe as it currently is but to look back in time and study galaxies and their CGM as they were and interacted billions of years ago by observing the light that comes from distant galaxies as it reaches us, after being redshifted as a consequence of the expansion of the Universe. These observations are easier to achieve if the targeted distant galaxy has a high luminosity. In general, there is a consensus that most galaxies host a supermassive black hole (SMBH) at their center (e.g., Kormendy & Richstone, 1995; Kormendy & Ho, 2013) with masses of $\sim 10^6$ - $10^{9.5}$ $M_\odot$. These SMBHs grow through the efficient accretion of gas. This is what we call an active galactic nuclei (AGN) phase, during which they become extremely powerful sources with higher luminosities ($L_{\rm bol} \approx 10^{48}$ erg s^{-1}) than normal star-forming galaxies, allowing the observation of active galaxies, such as quasars up to $z \sim 7.6$ (e.g., Bañados et al., 2018; Onoue et al., 2020; Wang et al., 2021).

[1]The virial radius of a galaxy is usually defined as the radius within which the mean density is 200 times the ambient density.

1.1. SMBH and galaxy host growth

The relation between the SMBH at the center of a galaxy and the host itself is tight but rather complex, with hints of co-evolutionary growth which is supported by the following observational evidence:

- The masses of the central SMBHs ($M_{\rm BH}$) are strongly correlated with the stellar velocity dispersion of their host galaxy bulges (σ) (e.g., Ferrarese & Merritt, 2000; Gebhardt et al., 2000; Tremaine et al., 2002; Gültekin et al., 2009), with the bulge luminosity (Kormendy & Richstone, 1995) and also with the mass of the bulge or spheroid of the galaxy (e.g., Magorrian et al., 1998; Häring & Rix, 2004). Interestingly, these relations have only been seen in ellipticals and galaxies hosting classical bulges (Kormendy & Ho, 2013). This is important because major mergers are likely to be the catalyst for the formation of classical spheroidals (Alexander & Hickox, 2012). The correlations of the $M_{\rm BH}$ with different properties of galaxy bulges imply a close connection between BH formation, galaxy formation, and AGNs.
- The observations of the star formation history (SFH) and accretion activity history of SMBHs have a similar peak and fall through cosmic time, reaching their maximum rate at $z \sim 2$ with a close relationship among all redshifts (see Madau & Dickinson, 2014, and references therein).
- Another piece of evidence comes when we analyze the relation between the luminosities associated with the star formation (SF) in the host galaxy ($L_{\rm SF}$) and the luminosity related to the SMBH accretion ($L_{\rm AGN}$). If $L_{\rm SF} > L_{\rm AGN}$, these properties are not correlated. However, when the systems are dominated by the accretion onto SMBH ($L_{\rm AGN} > L_{\rm SF}$), these quantities correlate by following a power law line (see Figure 13 of Netzer, 2009) which implies that the intense SMBH activity occurs at the same time that the SF activity, but that the AGN is not necessarily as its peak when the SF is happening. This could be explained because while SF proceeds in time scales of $\sim 10^7$ yrs, SMBH duty cycles are thought to be about one order of magnitude shorter. Models suggest that this behaviour of the BH growth introduces an observational de-correlation between SMBH and SF activity (Hickox et al., 2014; Volonteri et al., 2015).

In fact, the mass assembly of galaxies in early epochs of the Universe is expected to be a process driven by a combination of, at least, two main mechanisms that support the SMBH growth and SF of the host galaxy simultaneously. These mechanisms are the accretion of cold gas from the inter/circumgalactic medium (IGM/CGM) and the interaction between gas-rich galaxies known as mergers events (Kereš et al., 2005; Dekel et al., 2009; Bournaud et al., 2011). In the first scenario, the inflows of cold gas would provide new, almost pristine gas to fuel galaxies, enhancing their SF activity and feeding their central SMBH, which increases the AGN activity. The concept of gas accretion is supported by a number of indirect and diverse observational evidence which includes the G-dwarf problem (Van den Bergh, 1962; Schmidt, 1963) in which the metallicity distribution of G type stars in the solar neighbourhood does not agree with the chemical model of a "close box" and it is necessary to introduce the accretion of metal poor gas to match the data to the models.

Another evidence is the observed short gas depletion time-scales in galaxies, meaning that the amount of available gas would not be able to sustain the SF activity unless it receives an injection of external gas (e.g., Genzel et al., 2015; Schinnerer et al., 2016). Also, the total amount of stellar mass observed in galaxies is well matched by the integral of the SF across cosmic time (after accounting for the return of baryons to the ISM at the latest stages of stellar evolution), again implying that fresh supply of gas is required for the build up of currently observed galaxies (Walter et al., 2020).

In the merger scheme, it is expected to see a redistribution of the gas inside galaxies, concentrating it in the central regions where it feeds the SMBHs, and the increasing gas density trigger SF (e.g., simulations from Mihos & Hernquist, 1996; Springel et al., 2005). These close encounters leave imprints in the morphology of the interacting galaxies, as seen in the irregular shapes in the distribution of gas on circumgalactic scales. Particularly, it is observed that most of the extreme star-forming systems at high-z, and plenty of the most luminous AGN in the local Universe are associated with mergers (Sanders et al., 1988).

However, obtaining direct observations of both mechanisms at high-z is a challenge. In the inflow case, although it is hard to detect its emission due to the diffuse nature of the cold gas accreted, there is growing evidence for gas accretion from the CGM even to $z \sim 1$ (Bouché et al., 2016; Martin et al., 2019; Zabl et al., 2019). On the other hand, observations of merging systems at high-z are not only limited by the spatial resolution needed to resolve the structures but also by the obstacle of differentiating between the emission of the SMBH at the center and the galaxy host, when the AGN emission dominates the optical-NIR spectral regime erasing all properties of the host. Under this condition, the best approach is to look into the far-infrared (FIR) regime where the dust grains heated by young stars dominate the continuum emission and the host kinematics can be accessed by the observations of interstellar emission lines, such as [CII].

Carbon is one of the most abundant elements in galaxies, with [CII] arising from nearly every phase of the ISM due to its relatively low ionization potential (11.26 eV) (Lagache et al., 2018) including the neutral (HI) clouds, molecular gas and ionized phases associated with dense photodissociation regions (PDR) in the outer layers of molecular clouds (Hollenbach & Tielens, 1997; Wolfire et al., 2003). Additionally, the [CII] line is the brightest FIR emission line (Stacey et al., 1991), representing one of the most efficient coolants of the ISM. The measured transition frequency is 1900.537 GHz (Cooksy et al., 1986) corresponding to a transition wavelength of 157.74 μm, making the [CII] line observable for $4.5 \lesssim z \lesssim 8.5$ using sub-mm observations (band 6 and 7) of the Atacama Large Millimeter/submillimeter Array (ALMA).

1.2. Mergers

Since the advent of ALMA in 2011, several works have reported interacting systems beyond the local Universe, where the presence of companions increases in high-density environments (e.g., Decarli et al., 2019; Jones et al., 2019; Prochaska et al., 2019; Ginolfi et al., 2020; Romano et al., 2021; Banerji et al., 2021). These mergers are mainly identified based on the spatial projected separation of the galaxies involved ($\Delta d < 50$ kpc) and small velocity offset ($\Delta v < 500$ km s^{-1}), added to their perturbed morphologies with extended distributions of gas.

Furthermore, hydrodynamical simulations of minor and major mergers have contributed to understanding how these galaxies evolve during the interaction, mostly at low-z, even reproducing the observational states of some known major mergers (see Barnes & Hibbard, 2009, for a summary). Overall, the phases of a merger are well-identified, starting from a pre-merger state where a pair of galaxies start to approach and no significant evolution of the angular momentum can be appreciated. After that, the first passage or pericenter occurs, where galaxies reach their first close contact. In this phase, the angular momentum drops due to the gravitational and dynamical torques, which causes the flow of gas inwards, eventually increasing the SMBH activity and enhancing the SF (Prieto et al., 2021). This is expected to replicate during each of the following pericenter states. Commonly, depending on the specific nature of the galaxies, different types of tidal tails from the disks are formed after the first pericenter, especially visible in the apocenter phase (maximum separation of the galaxies) as seen in panel (e) of Figure 1.1 taken from Renaud et al. (2009), showing simulations of the merger evolution of the Antennae galaxies (NGC 4038 y NGC 4039; Arp 244). In the simulation, not only the tidal tails but the tidal bridge can be noticed, connecting both galaxies. After a number of consecutive passages, their SMBHs start to orbit each other until they eventually merged. Posterior to the merger state, the angular momentum is expected to return to constant with time, entering the final phase where the material is falling back into the merger remnant.

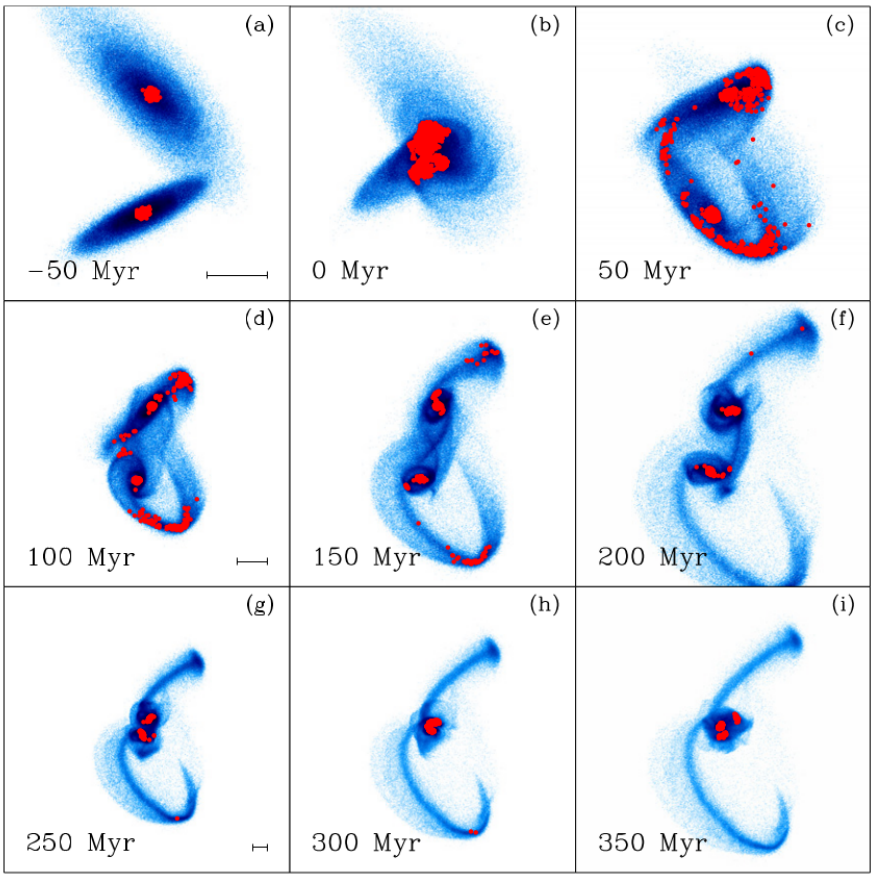

Figure 1.1: Figure 3 of Renaud et al. (2009). Morphology of the disks of the Antennae model every 50 Myr. On each row, the black line represents 10 kpc. t=0 (b) corresponds to the first pericenter. The tidal bridges and tails are created in the first 10 Myr after the first passage, while the galaxies move apart. The best match with observations is obtained at t $\approx$ 300 Myr (h). Red dots denote the particles standing in the fully compressive tidal mode.

1.3. This thesis

We investigate the dynamical state of J205724.14, an ongoing merger system composed by a quasar (QSO) at $z \sim 4.683$ and a companion dusty star-forming galaxy (DSFG) at a spatial distance of ~ 20 kpc ($3''$) in the south-east direction, which was referred as a sub-millimeter galaxy (SMG) in N20[2]. The sources were previously reported by Nguyen et al. (2020) (N20 hereafter) as part of a sample of twelve targets observed during ALMA Cycle 4 (project code 2016.1.01515.S) using the [CII] $\lambda \sim 157.74$ μm line and the underlying far-infrared (FIR) continuum at rest frame ~ 152 μm. The main source and its companion can be seen in Figure 1.2 as well as a source marked as "B", which was treated as a source only seen in projection in N20 because it has strong continuum emission but is not detected in [CII] and it is located $\approx 6.3''$ away from the quasar in the SE direction, which corresponds to a projected distance of ≈ 41.8 kpc at the redshift of the QSO.

In N20, properties for the continuum and [CII] emission were measured. The DSFG showed two components in [CII] labeled as E and W and two other components were detected in continuum emission, NE and SW. The location of the continuum and [CII] components did not match as can be seen in Figure 1.4. Additionally, there was a detection of a [CII] bright feature that consisted in a ~ 7 kpc extended "tidal-like" structure of debris material that extends beyond the quasar from east to west in a straight direction (see Figure 1.5). The continuum emission was not detected in this structure as can be seen in Figure 1.3 taken from N20. The [CII] line properties were not fully explored as the data used for their analysis had some limitations that will be discussed in Section 2.2. Therefore, further observations were required in order to determine the origin of this system.

Our goal is to study the circumgalactic environment of the J205724.14 system, including the extended emission, using new observations at $0.3''$ and $0.06''$ spatial resolution from ALMA Cycle 6 (project code 2018.1.01830.S) of the [CII] $\lambda \sim 157.74$ μm line and underlying FIR continuum at rest frame ~ 152 μm. Throughout this work we assume a cosmological model with $H_0 = 70$ km s^{-1} Mpc^{-1}, $\Omega_M = 0.3$ and $\Omega_\wedge = 0.7$ which gives an angular scale of 6.5 kpc/$''$ at $z = 4.6$. For the star formation rate (SFR) estimations we use a Chabrier initial mass function (IMF) from Chabrier (2003).

This thesis is organized as follows. In **Chapter 2**, we describe the data and the methods used for data reduction. We identify the components of the system and describe the methodology for spectral measurements. In **Chapter 3** we study the [CII] spectra and the continuum emission of our sources as well as estimate the spectral energy distributions (SED) and SFRs. In **Chapter 4** we estimate the dynamical, dust, and gas masses of the QSO host galaxy and the DSFG. We compare our results with the Schmidt-Kennicutt relation (SK) and also with the main sequence (MS) of galaxies after estimating the stellar masses. In **Chapter 5** we discuss the nature of the system as a major merger event based on our findings. Finally, **Chapter 6** concludes our thesis, summarizes the results, and discusses further work.

[2]We choose to label the companion a dusty star-forming galaxy (DSFG) instead of a sub-millimeter galaxy (SMG) as the continuum flux density of this source is approximately half of the flux expected for an SMG, this is $S_{850} >$ 3-5 mJy. The actual continuum flux of this source is 1.4 mJy as reported in Section 2.3.

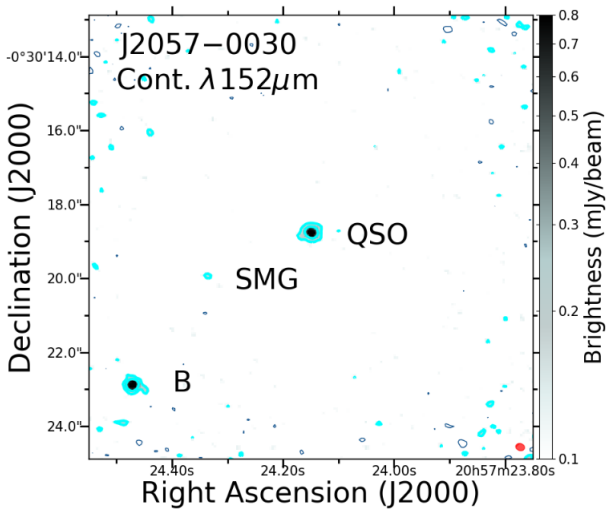

Figure 1.2: Figure 1 of Nguyen et al. (2020). The gray-scale maps show the continuum emission. The cyan (blue) contours trace emission at different positive (negative) significance levels. The first contour traces the region where the continuum emission exceeds 2σ, and consecutive contours are plotted in steps of 2σ. The beam is shown as a red ellipse at the corner. The source labeled as "B" lacks significant [CII] emission and it is expected to be a source only seen in projection.

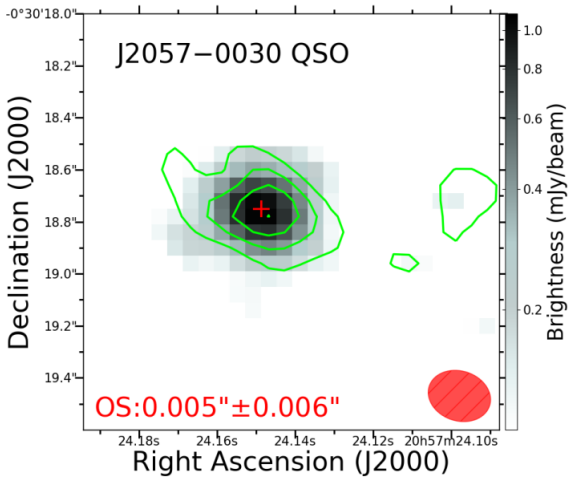

Figure 1.3: Figure 3 of Nguyen et al. (2020). The gray-scale map traces the continuum emission, while the contours trace the [CII] line emission at significance levels of 3, 6, 9, and 12σ. The beam is shown as a red ellipse near the bottom-right. The optical position from GAIA is marked with a red cross (+). The main source (QSO) shows significant continuum and [CII] emission meanwhile the "extended feature" is only detected in [CII].

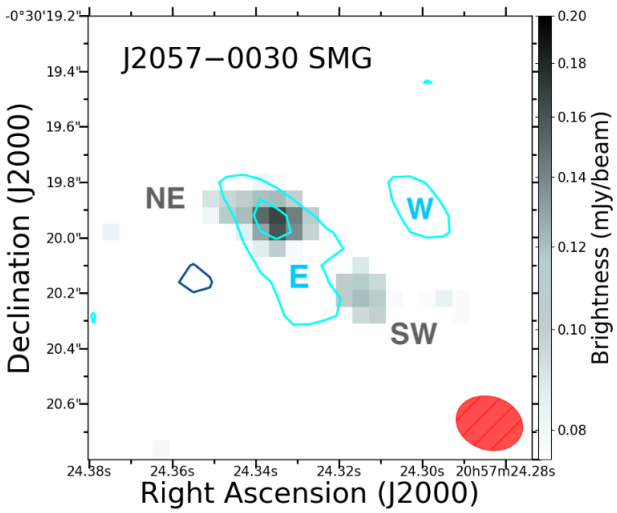

Figure 1.4: Figure 1 of Nguyen et al. (2020). The gray-scale map traces the continuum emission, while the contours trace the [CII] line emission at significance levels of 3, 6, 9, and 12σ. The beam is shown as a red ellipse near the bottom-right. The two components of the dusty star-forming galaxy (DSFG), labeled in N20 as a sub-millimeter galaxy (SMG) are observed in [CII] emission and labeled as E and W, while the two components seen in continuum are labeled NE and SW.

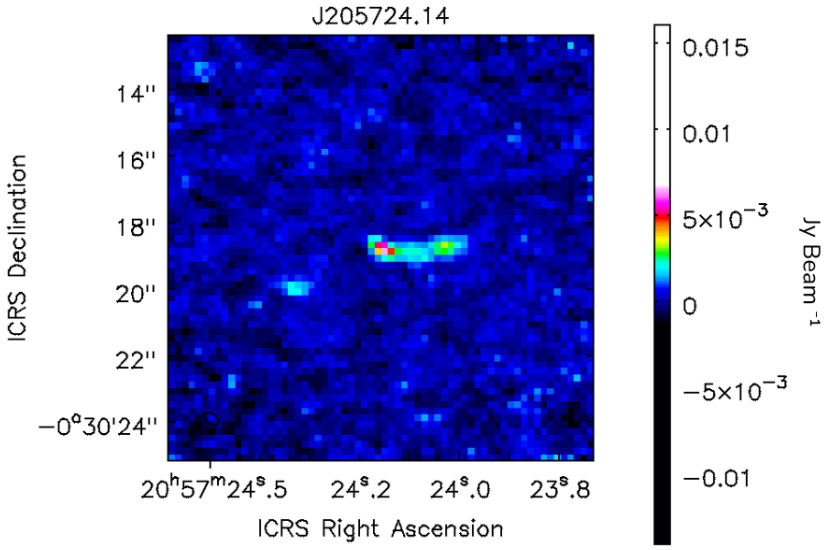

Figure 1.5: Narrow (1 channel), intensity map of the quasar and its tidal tail. The extended $\sim$ 7 kpc, "tadpole-like" structure is clearly seen. The dusty star-forming galaxy (DSFG) is also visible.

Chapter 2

ALMA observations and data reduction

2.1. Campaign background

This thesis will examine the $z \sim 4.68$ quasar J205724.14. The parent sample of J205724.14 was defined as a flux-limited sample in a narrow redshift bin. This strategy isolates the brightest objects at a particular cosmological epoch. Since the most powerful quasars at high-z are most likely the progenitors of the most massive galaxies at $z \sim 0$, samples like this will anchor models and theory of quasar and host co-evolution of the most massive galaxies known. The sample is based on the 38 brightest unobscured quasars from the sixth data release (DR6, Adelman-McCarthy et al., 2008) of the Sloan Digital Sky Survey (SDSS, York et al., 2000) at redshifts $z \sim 4.65$ - 4.92. MgII line λ2798 and the continuum flux at 3000Å (F_{3000}) were measured using VLT/SINFONI and Gemini-North/NIRI and used for black hole mass determinations. Results are presented in Trakhtenbrot et al. (2011) with estimations for the SMBH masses ($M_{\rm BH}$) in the range of $10^8 \lesssim M_{\rm BH} \lesssim 6.6 \times 10^9$ $M_\odot$ with a median of $\sim 8.4 \times 10^8$ $M_\odot$ and accretion rates of the quasars ($L/L_{\rm Edd}$) in the range of $0.2 \lesssim L/L_{\rm Edd} \lesssim 3.9$ with a median of ~ 0.6.

Additional observations by Herschel Spectral and Photometric Imaging Receiver (SPIRE) were presented in Mor et al. (2012) and Netzer et al. (2014) and relied on data from the Spitzer Infrared Array Camera (IRAC) (also from Netzer et al., 2014) 3.6 and 4.5 μm bands for positional priors for the Herschel photometry. The sources detected by Herschel/SPIRE instrument are denominated FIR-Bright sources with luminosities of $L_{\rm FIR} \sim 8.5 \times 10^{46}$ erg s^{-1} (2.2×10^{13} $L_\odot$) suggesting SFRs in the range $\sim$ 1000 - 4000 $M_\odot$ yr^{-1}, meanwhile the undetected quasars are classified as FIR-Faint sources with a median SFR ~ 400 $M_\odot$ yr^{-1} as calculated in Netzer et al. (2014) after a stacking analysis. In Trakhtenbrot et al. (2017) ALMA observations of six of these luminous quasars were reported but it is only in N20 where J205724.14 is presented using ALMA data. J205724.14 is classified as a FIR-Faint source with a luminosity of $L_{\rm FIR} \sim 10^{46.83}$ erg s^{-1}, accretion rate of $L/L_{\rm Edd} \sim 0.89$ and an estimated SMBH mass $M_{\rm BH} \sim 10^{9.23}$ $M_\odot$ as reported in Trakhtenbrot et al. (2011).

2.2. ALMA observations

In N20, the system was observed with ALMA band-7 (275 – 373 GHz) during Cycle 4. The C40-5 configuration was used (baselines $\sim$ 15.1 m - 1.1 km) in 2 execution blocks, one on 2017 May 02 and one on 2017 May 03. The number of antennas used in each case is 39 and 44, respectively. The on-source time was approximately 28 minutes per block. The observed angular resolution was 0.189″. J2232+1143 was used for band-pass and pointing calibration, J2148+0657 was used as a flux calibrator and the source J2101+0341 was used as a phase calibrator.

The spectral setup consisted of two sidebands separated by about 12 GHz, each constructed of two spectral windows (SPWs) of width 1875 MHz, which corresponds to $\sim$ 1650 km s^{-1} at the observed frequencies. For each SPW, this spectral range is sampled by 128 channels with a frequency of 15.625 MHz or $\sim$ 15 km s^{-1} per channel. Two of the spectral windows were centered on the frequency corresponding to the expected peak of the [CII] line, estimated from the MgII-based redshift determined in Trakhtenbrot et al. (2011). The other two adjacent windows were placed at higher frequencies and used for continuum measurements. Each of these pairs of spectral windows overlapped by roughly 50 MHz. The issue with this configuration emerged in a common flagging procedure during ALMA data reduction process when a few channels at the edge of the windows were rejected due to divergent flux values leading to a small spectral gap between pairs of windows. Unfortunately, the [CII] emission of all the sources present in J205724.14 lays in the middle of the gap, resulting in the loss of spectral information (see Appendix A).

Nonetheless, with Cycle 4 the QSO was clearly detected in [CII] and continuum emission. Close to the QSO, in the SE direction, a companion dusty star-forming galaxy (DSFG) was detected in [CII], with a morphology that appeared to be composed of two different components which were labeled as E (east) and W (west) based on their location. The DSFG showed another two different components in the continuum which did not match with the position of the ones showed in [CII], they were labeled as NE (northeast) and SW (southwest). The DSFG was previously referred to as a sub-millimeter galaxy (SMG) in N20. The QSO host and the DSFG were considered to be ongoing a merger event due to their small spatial separation and the perturbed morphology of the main source. The QSO host showed a strong [CII] emission that extended from east to west in a straight projection. This feature was not detected in continuum and was considered to be a tidal tail from the interaction of the QSO host and a its companion.

In our analysis, we count with new low and high spatial resolution observations obtained with ALMA band-7 obtained during Cycle 6. The 0.3″ low resolution data was taken using the C43-4 compact configuration (baselines $\sim$ 15.1 m - 740.5 m), 46 antennas, and an on-source time of roughly 19 minutes. For the high resolution data, the C43-7 array configuration was used (baselines $\sim$ 41.4 m - 3.4 km), during 2 execution blocks, one on 2019 August 21 and the other on 2019 August 23. The number of antennas was 44 for both cases and the on source time was 40 minutes per block, resulting in an angular resolution of 0.06″. In this cycle, J2253+1608 was used for flux, band-pass, and pointing calibration and the source J2101+0341 was used for pointing and phase calibration.

For both resolutions, the spectral setup consisted of two sidebands separated by about 12 GHz, each constructed of only one SPW. For the [CII] emission line window, the FDM correlator mode was selected covering an effective bandwidth of 1875 MHz, which corresponds to $\sim$ 1650 km s^{-1}. This spectral range is sampled by 3840 channels with a frequency of 0.488 MHz or $\sim$ 0.437 km s^{-1} per channel (high spectral resolution). For the continuum spectral window, the TDM correlator mode was used with the same configuration as Cycle 4 SPWs, covering an effective bandwidth of 1875 MHz, which corresponds to $\sim$ 1650 km s^{-1}. This spectral range is sampled by 128 channels with a frequency of 15.625 MHz or $\sim$ 15 km s^{-1} per channel.

2.3. Data reduction

Data reduction was performed using the CASA package version 5.6.1 (McMullin et al., 2007) and the visibilities were recovered with the scripts provided by ALMA. The line-free SPWs of every set of data at different spatial resolutions (Cycle 4 0.189″, Cycle 6 0.3″ and Cycle 6 0.06″) were separated from the windows that contain the [CII] line and they were concatenated into a single measurement set (MS file) using CONCAT command. The line-free file was taken to create the continuum images. For the [CII] line cubes, the continuum emission was subtracted independently with UVCONTSUB for each of the SPWs that contains the line in each of the different resolution data sets and then they were concatenated into one MS using CONCAT.

At first, we aimed to combine the low and high resolution observations from Cycles 4 and 6. For this, we started combining the continuum subtracted data that was stored in one MS file, creating the [CII] emission line cubes using the TCLEAN algorithm, which was run using "briggs" weighting and robust = 2.0, in order to obtain the best signal to noise value (taking advantage of the high resolution data available). However, TCLEAN had difficulties interpolating the flux in Cycle 4 when combined with Cycle 6, generating a "false" peak in the frequency range covered by the gap. To avoid this issue, we performed the cleaning after recovering the rejected channels at the edge of the windows and this time the interpolation was successful with no presence of a false peak but the newly added channels seem to be of low quality and a particularly strange pattern of noise appeared in the channels of the cubes hindering the creation of the [CII] moments. For these reasons, Cycle 4 data was discarded from the following analysis.

We repeated the procedure of combining the [CII] line data and also the continuum data using CONCAT command but this time only with the Cycle 6 low and high resolution observations. For the line cube, we averaged the flux distributed in 3840 channels by using TCLEAN command with a width = 54 km s^{-1} reducing the number of channels to 30. We also applied a "briggs" weighting, robust = 2.0 and restoringbeam parameter set to "common" for [CII] line cubes and line-free images. By using the restoringbeam parameter we tried to fit a common size and shape to the beam in all the planes. Unexpectedly, the beam size for the continuum and [CII] emission line cubes did not match. The line-free cube had a beam size of 0.12″ $\times$ 0.09″ at a Position Angle (P.A.) = -52.96°, closer to the beam size of

$0.11'' \times 0.08''$ at a P.A. = -51.2° of the high resolution cubes ($0.06''$). Meanwhile, the [CII] line cube ended up with a beam of $0.41'' \times 0.36''$ at a P.A. = -35.69°, which is similar to the beam size of $0.42'' \times 0.38''$ at a P.A. = -34.51° of the low resolution data ($0.3''$). To investigate these results, we also ran TCLEAN with restoringbeam off and the resulting cubes showed a different range of varying beam sizes among the planes, which mean values were $0.14'' \times 0.10''$ at a P.A. = -65.64° for the [CII] line cube and $0.14'' \times 0.10''$ at a P.A. = -66.48° for the continuum cube, these values were considered the "native" resolution of the combination with both being closer to the high resolution beam size. However, these beam sizes were very small and not optimal to measure quantities as the flux densities or to calculate the moments maps. Hence, in order to explore the spatial distribution of the sources in detail and also measure their spectral properties we finally used two restoringbeam parameters to have cubes with two different spatial resolutions.

The first beam size was set to $0.41'' \times 0.36''$ at a P.A. = -35.69° which is closer to the low resolution beam size and equal to the final beam of the [CII] line cube when restoringbeam was set to "common" and it seems to provide a convenient compromise between resolution and S/N (See left panel of Figure 3.3). The other chosen beam size was $0.16'' \times 0.12''$ with the same P.A of the low resolution, allowing multiscale analysis of our sources (See right panel of Figure 3.3). Each configuration is identical for [CII] cubes and continuum images.

The properties for the continuum emission were obtained by collapsing the line-free cube into one channel. Figure 2.1 shows the continuum map of the system with the [CII] emission contours at a significance level of [2, 2.5, 3, 3.5, 4, 5, 8] σ where $\sigma_{[CII]} = 0.218$ Jy km s^{-1} beam^{-1}. In the left panel, the QSO and the source "B" have the strongest continuum emission. The QSO flux is 2.4 mJy with a S/N $\approx$ 10 and "B" has a continuum flux of 3.2 mJy and a S/N $\approx$ 9. The DSFG is less noticeable with an emission of 1.4 mJy and a S/N $\sim$ 4.5.

2.4. Source detection

2.4.1. [CII] emission

Based on the Cycle 4 [CII] line observations, N20 identified the presence of three components in the system J205724.14: The main source which is the quasar (QSO), the second brightest source which corresponds to the dusty star-forming galaxy (DSFG), previously identified as a SMG in N20. The final component is the extended emission which was referred as the "tidal tail". In this analysis, based on Cycle 6 observations of the [CII] line emission, we detected the quasar, the DSFG and the extended emission but this time, the "tail" breaks into three distinct clumps projected in an almost straight East-West direction from the QSO. They are labeled from east to west as C1, C2 and C3, as can be seen in Figure 2.3, which shows the integrated flux of the spectrum map (Moment 0) of the [CII] line. The clumps have their [CII] integrated flux detected at $\sim$ 8, 6, 5σ[1], respectively. C3 corresponds to a narrow feature with a FWHM $\sim$ 82 km s^{-1}. Considering that the width of the cube channels

[1]The signal-to-noise (S/N) was calculated as the integrated value of the [CII] divided by the squared sum of the noise over the integrated range of the spectrum of $\pm$ 3σ ($F/\sqrt{\sum_i n_i^2}$).

is 50.3 km s^{-1}, the line corresponds approximately to one channel of the cube and it was identified when a map of the peak flux of every spaxel was plotted, as seen in Figure 2.4. We also detect a new possible component, a fourth clump labeled as C4, detected at $\sim 8\sigma$ in the south-west direction and it is the furthest clump detected at a distance of $\sim$ 28 kpc from the QSO.

In addition to our six main components, we also detect two fainter clumps to the west of the DSFG, which we refer to as S0 and S1 (see Figure 2.3) with their [CII] integrated fluxes detected both at $\sim 6\sigma$. Through this work, we will discuss the possibilities of them being real sources acting as a "tidal bridge" connecting the DSFG to the quasar in a merging scenario.

Source "B" previously reported by N20 as a source only seen in projection is also detected in this work, showing the same pattern as in N20 with a strong continuum emission but no detection of [CII]. The hypothesis of "B" not being part of the system is supported by the argument that if "B" was an actual component, at the same redshift, the distance to the QSO would be $\sim 6.3''$ or $\sim$ 42 kpc, this is two times the distance of the QSO-SMG. Even if the system was this extended, the [CII] emission of "B" should be very faint (fainter than the emission of the clumps) in order to not be detected, which would yield a high upper limit for the $L_{\rm CII}/L_{\rm FIR}$ ratio (see Section 3.3), with an extreme [CII] deficit for a source with a FIR luminosity $\log L_{\rm FIR} \sim 12.68 \pm 0.06\ L_{\odot}$. However, the non-detection of [CII] in "B" could represent a larger velocity offset with respect to the QSO (700 km $s^{-1} < \Delta_v <$ -900 km s^{-1}), and as our SPWs cover a width of $\sim$ 1500 km s^{-1} we might not be able to detect it and therefore the amount of [CII] in this source remains unknown. Showing a large velocity shift would be in agreement with having a large spatial separation with respect to the QSO. For these reasons, we are not able to conclude if "B" is part of the system and therefore we report its continuum emission but we do not include it in the discussion of the physics of the system.

2.4.2. Continuum emission

Using the CASA viewer tool we fitted a 2D Gaussian to the QSO and "B" source. We adopted these values to characterize the sizes of the continuum emitting regions and used them to set the elliptical apertures for the flux determinations over the line-free image. The purpose of the fit is to subtract the QSO and "B" emission from the continuum image. This improves the visualization of the fainter sources, such as the DSFG and clumps, against the background. This image was not used for flux measurements. The result is seen in Figure 2.1 right panel, where the limits of the colorbar had been adjusted in order to highlight the emission of the DSFG, which shows an interesting extended morphology (see the right side of Figure 2.2). In fact, in N20 the DSFG has two components labeled as NE and SW according to their position, which are in good agreement with the strongest emission perceived in our case, which is aligned in that direction. Figure 2.2 also shows more low surface brightness emission that extends to the South and may be a part of the source. However, it is not possible to confirm its detection with the available S/N as the emission does not truly stand out from the background.

Because of the faint extended emission at the South of the DSFG, the 2D Gaussian fit of the continuum emission is larger than that for [CII], where the line emission of the DSFG is more rounded and the extra emission surrounding it is considered to be two different clumps (S0 and S1) that are fitted independently. It is important to remark that the location of the [CII] clumps poorly match the distribution of the continuum extended emission, as only the S0 clump might partially coincide with one of the fuzzy "tails" seen in the continuum.

This behavior of the DSFG with a larger extension for the star-forming region than [CII] emission is the opposite of what has been seen in the literature for sources at high redshift ($z > 4$) (e.g., Fujimoto et al., 2019; Carniani et al., 2020) where the [CII] region is more extended than the UV region dominated by star formation, which in our case, is traced by the FIR continuum. A more complete determination of the morphology of the DSFG in dust continuum and [CII] emission will require deeper observations.

For the QSO (left panel of Figure 2.2) the continuum emission is remarkable compared to that of its neighbouring clumps, which have no continuum emission. These results are in agreement with N20 which previously reported no continuum emission in the tidal tail. However, it is worth mentioning that the higher continuum flux is shown by C3, with 0.48 mJy and a S/N $\sim$ 2.5, this is interesting because C3 has the lower [CII] integrated flux. The clumps close to the DSFG (S0 and S1) are also not detected in the continuum.

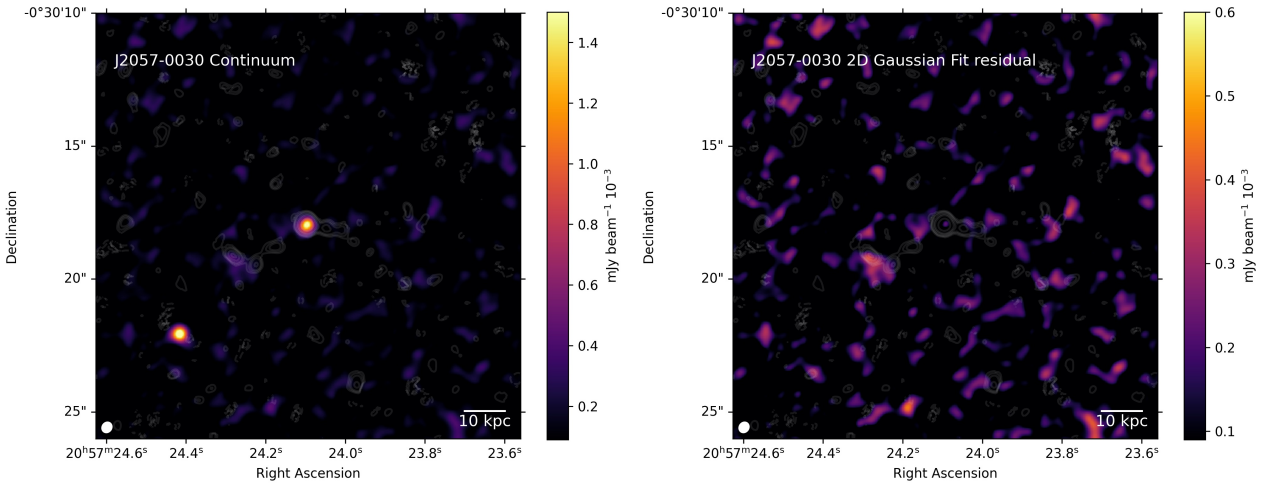

Figure 2.1: Left: Continuum emission image. The QSO has significant emission as well as the source "B" which has no [CII] emission and as Nguyen et al. (2020) mentioned it seems to be a source only seen in projection. The DSFG shows faint continuum emission. Right: Continuum image after the QSO and the "B" source have been fitted by a CASA 2D Gaussian fit and has been subtracted from the original image. Both panels have the [CII] contours overplotted as white solid (dashed) contours indicate the positive (negative) significance levels at [2, 2.5, 3, 3.5, 4, 5, 8] σ. The synthesized beam is shown at the bottom-left corner as a white filled ellipse. North is up and east is to the left.

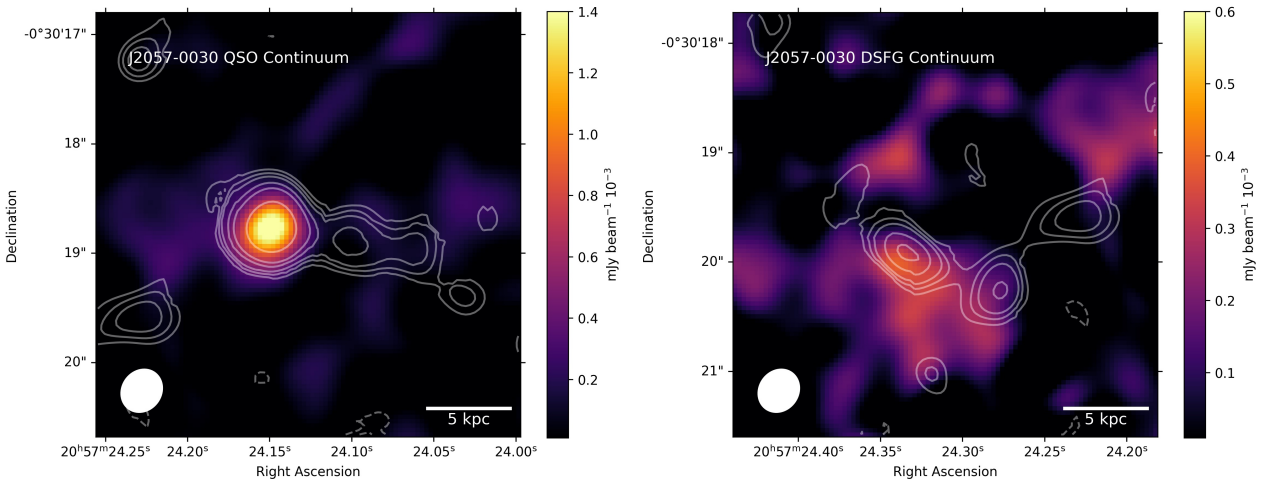

Figure 2.2: Continuum emission with [CII] contours over-plotted as white solid (dashed) contours indicate the positive (negative) significance levels at [2, 2.5, 3, 3.5, 4, 5, 8] σ. Left: QSO continuum emission image plus the nondetected clumps C1, C2 and C3. Right: DSFG continuum image with the neighbouring clumps, S0 and S1. The synthesized beam is shown at the bottom-left corner as a white filled ellipse. North is up and east is to the left.

2.5. Continuum and spectral measurements

Using the low resolution continuum image we estimate the FIR continuum fluxes of the sources with two approaches depending on the source. In the first case, we calculate the sizes of the continuum regions of the main component QSO and the DSFG by fitting a CASA 2D Gaussian, which is characterized by a peak flux, semi-major and semi-minor axes, and a position angle. The fluxes of the quasar and its companion were measured by integrating over the beam-convolved sizes given by the 2D Gaussian. For the remaining components, CASA could not fit a spatial 2D Gaussian as the emission of the sources was too weak. Then, the fluxes were obtained directly from the continuum images using elliptical apertures based on the [CII] extension of the sources (as seen in moment 0).

Using the continuum subtracted [CII] emission line cubes we calculate the zero, first and second moment corresponding to the integrated value of the spectrum, the velocity fields and velocity dispersion fields, respectively. To create them, we used two methods. First, we used the python package LMFit to fit a Gaussian profile along the velocity axis of every spaxel in the cube using three free parameters: the amplitude (I_0), the standard deviation (σ) and the center of the Gaussian (x_0). Then, we applied moment equations directly over the spectral values enclosed in $\pm 3\sigma$, with σ from the Gaussian best fit, as this range is expected to include $\sim$ 99.73 % of the total flux of the spaxel. Second, we calculated the velocity and velocity dispersion fields using the values of the free parameters obtained from the Gaussian fit. In the case of moment 1, we used the value of the center of the Gaussian x_0 as the velocity of the spaxel and for moment 2, we use the values for the parameter σ as the velocity dispersion. The results between the two methodologies are quantitatively and qualitatively in good agreement. For this reason, in the following sections we will discuss the kinematics of the sources based on the first approach, using the moments obtained by applying the equations

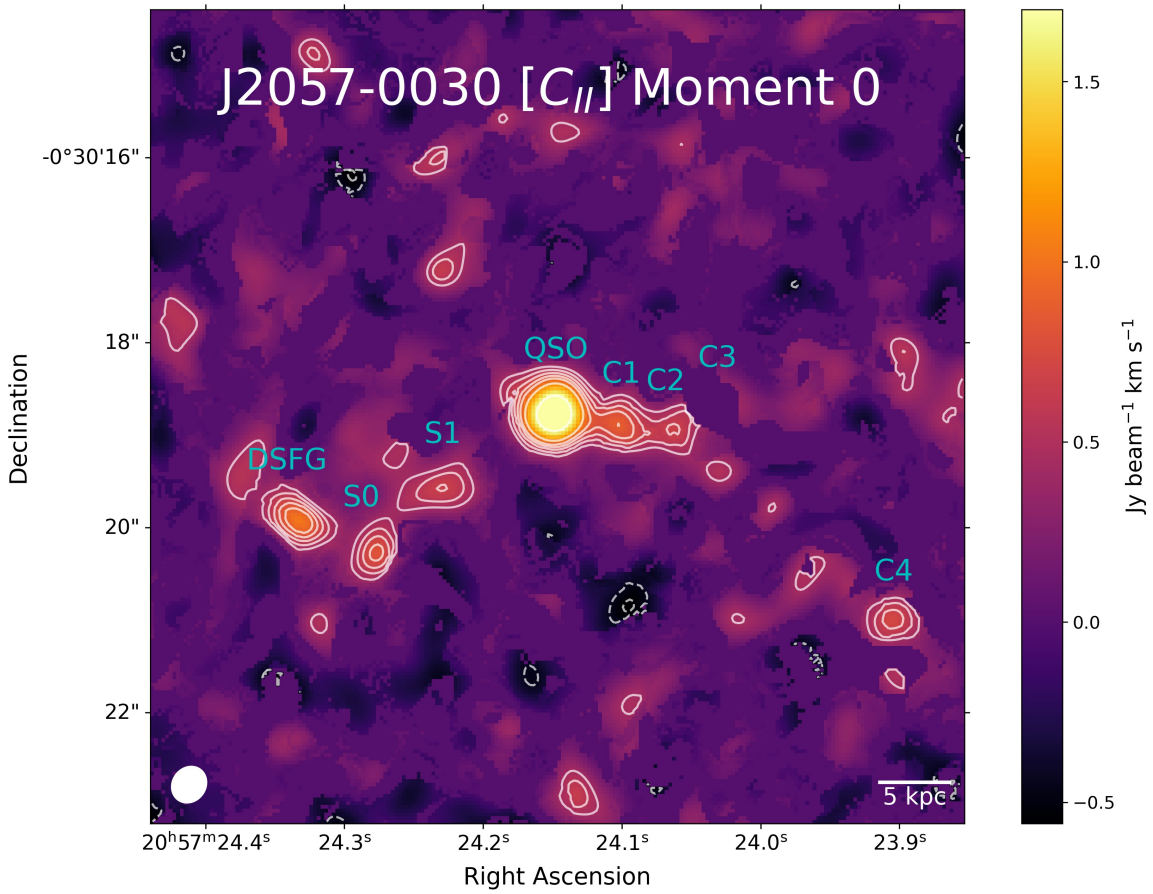

Figure 2.3: The map is showing the integrated value of the [CII] spectrum (moment 0) for the lower resolution combination. White solid (dashed) contours indicate the positive (negative) significance levels at [2, 2.5, 3, 3.5, 4, 5, 8] σ. The synthesized beam is shown in the bottom-left corner as a white filled ellipse. North is up and east is to the left.

over the $\pm 3\sigma$ spectral range taken from the Gaussian fit as we try to avoid an over-fitting of the spectra in the spaxels dominated by the background emission.

We used the moment zero map to estimate the sizes of the [CII] regions by fitting a CASA 2D Gaussian for each component of the system, except for C3 which is our narrowest feature (see Section 2.4), only weakly noticeable in moment zero so the software could not detect it. Therefore we used an elliptical aperture based in our visual estimation of its [CII] extension. The [CII] and continuum beam-deconvolved sizes of the sources are reported in Table 3.1 with the uncertainties estimated using Monte Carlo simulations. We define the elliptical apertures to extract the 1D spectra with a radius of 2σ based on the 2D Gaussian estimation of the beam-convolved size of the components, representing $\sim$ 86.47% of the total flux of the sources if their spatial flux distributions is well described by a 2D Gaussian. The sizes of the apertures were chosen in order to avoid the spatial overlapping of the main sources and clumps. To estimate the line fluxes we fit a Gaussian profile to the [CII] spectrum using LMFit and then integrated over the line covered by $\pm$ 3σ.

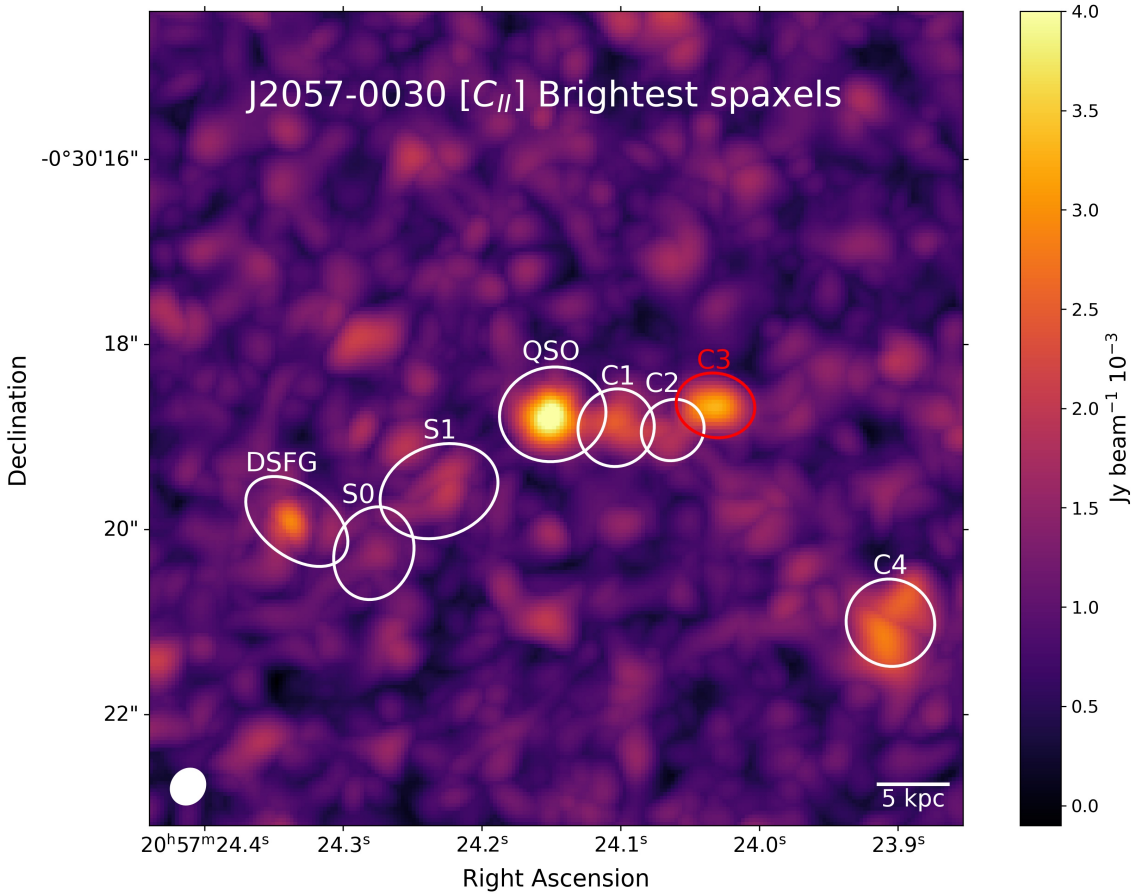

Figure 2.4: The map is showing the brightest spaxel value of the [CII] spectrum for the lower resolution combination. The red ellipse represents the clump C3 which is only noticeable in one channel as it has a narrow FWHM $\sim$ 82 km s^{-1}. The white ellipses represent the rest of the components analyzed in this work: The quasar (QSO), the dusty star-forming galaxy (DSFG) and the clumps: C1, C2, C4, S0 and S1. The synthesized beam is shown in the bottom-left corner as a white filled ellipse. North is up and east is to the left.

2.6. Calibration Issues

Visual inspection of the obtained spectra showed significant differences in the peak and integrated [CII] emission of sources when comparing data obtained at different resolutions, with a higher flux found in the combined data of both Cycle 6 configurations. The same issue was observed in the continuum fluxes. We looked for flux calibration issues but no evident problems were found. We explored the possibility of this result being caused by the "JvM" effect (see Czekala et al., 2021). The "JvM" effect (first described in Jorsater & van Moorsel, 1995) is caused by the mismatched units between the model image and the residual image that form the restored (cleaned) image after the cleaning process in CASA. The smaller beam of the image model compared with the dirty beam (i.e., as DIRTY BEAM $>$ CLEAN BEAM, Jy DIRTY BEAM^{-1} $<$ Jy CLEAN BEAM^{-1}), results in a significantly higher flux in the clean image. To test if the flux difference was caused by the "JvM" effect, we subtracted the residual image from our cleaned image to measure the remaining flux. The resulting image still exhibited a significant increase in flux (without residuals) implying that the "JvM" effect could not explain the discrepancy.

We further compared the QSO continuum flux obtained by N20 from Cycle 4 with the flux found from our low and high resolution data from Cycle 6. Using the continuum emission avoided problems of contamination from the nearby clumps. A difference of ~ 10 % and ~ 25 % was found, respectively. As a ~ 10 % error is considered as a typical accuracy for ALMA data, and the emission from our sources should not vary with time, we assumed that the low resolution data give the correct flux values and that a yet to be discovered issue (such as fast variability of the quasars used as ALMA calibrators) is affecting the high resolution data. Therefore, we scaled the fluxes in the combined [CII] cubes and continuum images using a scaling factor that allowed us to reach the level of flux seen in the low resolution data.

Chapter 3

[CII] line and dust emission properties

3.1. [CII] line properties

We extract the 1D spectra of our components using elliptical apertures based on the beam-convolved sizes from the 2D Gaussian fit of the [CII] emission, as seen in Figure 3.1 in white, and which correspond to the 6 main components analyzed in this work: The quasar (QSO), the sub-millimeter galaxy (DSFG) and the clumps C1, C2, C3 and C4. The red ellipses correspond to the two regions detected close to the DSFG, S0 and S1. Finally, the blue ellipses seen in Figure 3.1 represent the 2D Gaussian fit of the continuum emission for the two main sources. The QSO and the DSFG are slightly resolved, meanwhile the rest of the components have sizes comparable to the beam.

Figure 3.2 shows the [CII] line spectra of the sources as blue step plots, while overplotted Gaussian fits are shown as a solid red line. Zero velocities correspond to the peak intensity of the quasar fit. The rms of the channels are shown as gray bars. For the QSO the [CII] line covers a wide range of frequencies with a FWHM $\sim$ 345 km s^{-1} and a peak of $\sim$ 11 mJy, in good agreement with N20. The spectrum is not completely symmetric showing slightly more flux at higher velocities ($\sim$ 200 km s^{-1}) but we notice that a single Gaussian fit still works better for this spectrum than fitting two components.

The DSFG spectra indicates a velocity shift with respect to the QSO's systemic redshift of about $\sim$ -68 $\pm$ 15 km s^{-1} representing a difference in their redshifts of $\Delta z \approx 0.002$. This small velocity offset reinforces our idea of an interaction between the QSO and the DSFG as is comparable (and smaller in some cases) than other shifts seen in ongoing merger systems at high-z (e.g., Jones et al., 2019; Ginolfi et al., 2020; Romano et al., 2021, all from ALPINE (the Atacama Large Millimeter/submillimeter Array (ALMA) Large Program to INvestigate [CII] at Early times). The spectrum of the DSFG centered at the Zero velocity of the Gaussian fit to the DSFG itself is plotted as an orange line in Figure 3.2. The emission consists of a main peak of $\sim$ 5 mJy at $\sim$ 0 km s^{-1} at and a presumably smaller peak of $\sim$ 2.5 mJy at $\sim$ 300 km s^{-1}.

The clumps C1, C2 and C3 show velocity offsets with respect to the QSO of $\sim$ -39 $\pm$

11 km s^{-1}, $\sim$ -24 $\pm$ 15 km s^{-1} and $\sim$ -51 $\pm$ 7 km s^{-1}, respectively, suggesting that all of them are gravitationally connected to the quasar. Meanwhile, C4 shows the most extreme offset in velocity with $\sim$ 112 $\pm$ 12 km s^{-1} which coincides with the fact that this is the most spatially separated clump from the QSO. Still, its velocity offset is comparable to that of the DSFG. In the case of C1, the spectrum shows a similar shape to the main source with a very tentative secondary peak of $\sim$ 2 mJy at velocities $\sim$ 200 km s^{-1} as seen in the QSO case. For C2, the shape of its emission seems more asymmetric than the rest of the clumps with a notable rather narrow peak of $\sim$ 3 mJy at $\sim$ 0 km s^{-1} and a possible small secondary component at $\sim$ 200 km s^{-1}. In C3 the Gaussian fit presents the poorest result as the emission of the clump is very narrow with a peak of $\sim$ 6 mJy covering only a few km s^{-1} (one channel).

S0 and S1 show velocity shifts with respect to the QSO's systemic redshift of $\sim$ 181 $\pm$ 31 km s^{-1} and $\sim$ 116 $\pm$ 39 km s^{-1}, respectively. If we compare their velocities to the DSFG's systemic redshift we get a velocity offset of $\sim$ 249 $\pm$ 31 km s^{-1} and $\sim$ 184 $\pm$ 39 km s^{-1}. Deeper observations are required to probe their velocity maps.

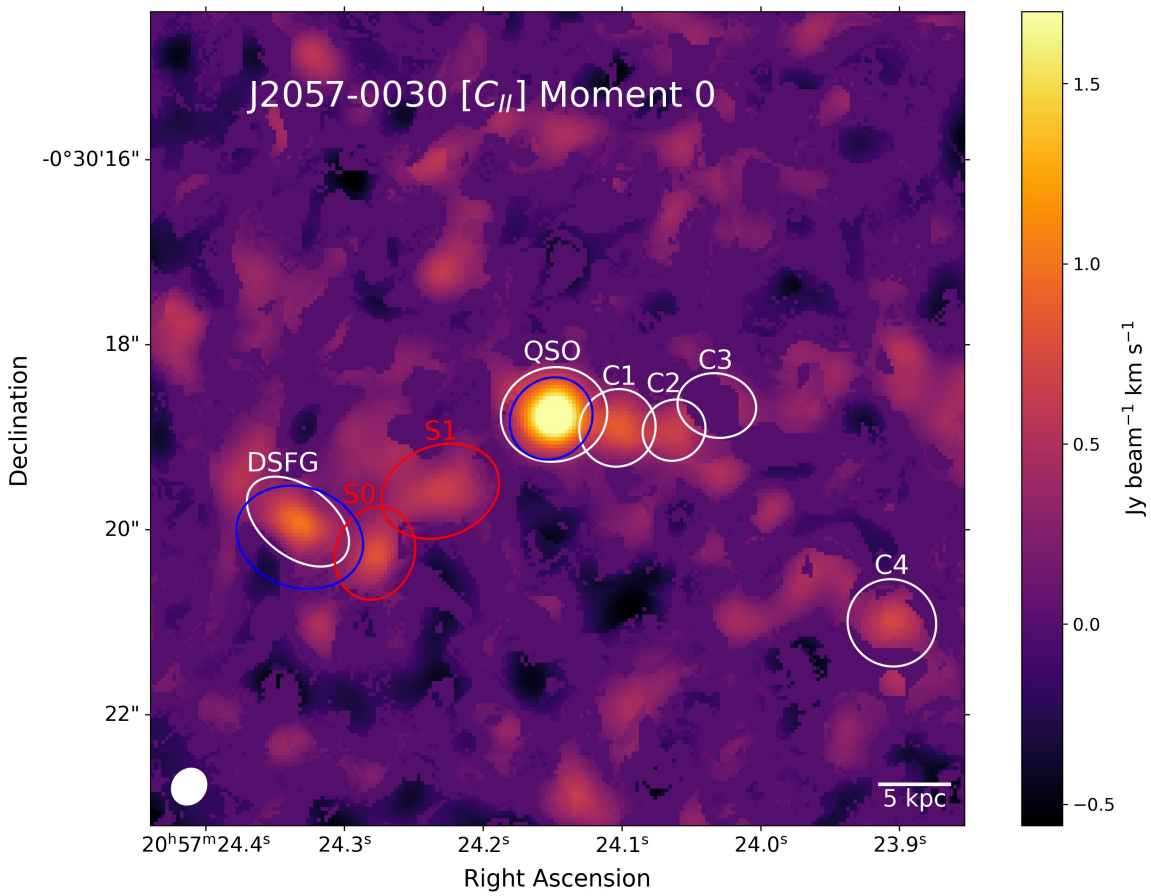

Figure 3.1: Apertures used to measure the fluxes of the sources. The map is showing the integrated value of the [CII] spectrum (moment 0) for the lower resolution combination. The white ellipses represent the 6 main components analyzed in this work: The quasar (QSO), the dusty star-forming galaxy (DSFG) and the clumps: C1, C2, C3, and C4. The red ellipses are two strong emissions possibly representing real sources connecting the DSFG and the quasar (S0 and S1). The white and red apertures are used to extract the [CII] 1D spectra of all the sources and to measure the continuum emission for the clumps. The continuum of the QSO and DSFG was estimated using the blue ellipses representing the 2D Gaussian fit of the continuum. The synthesized beam is shown in the bottom-left corner as a white filled ellipse. North is up and east is to the left.

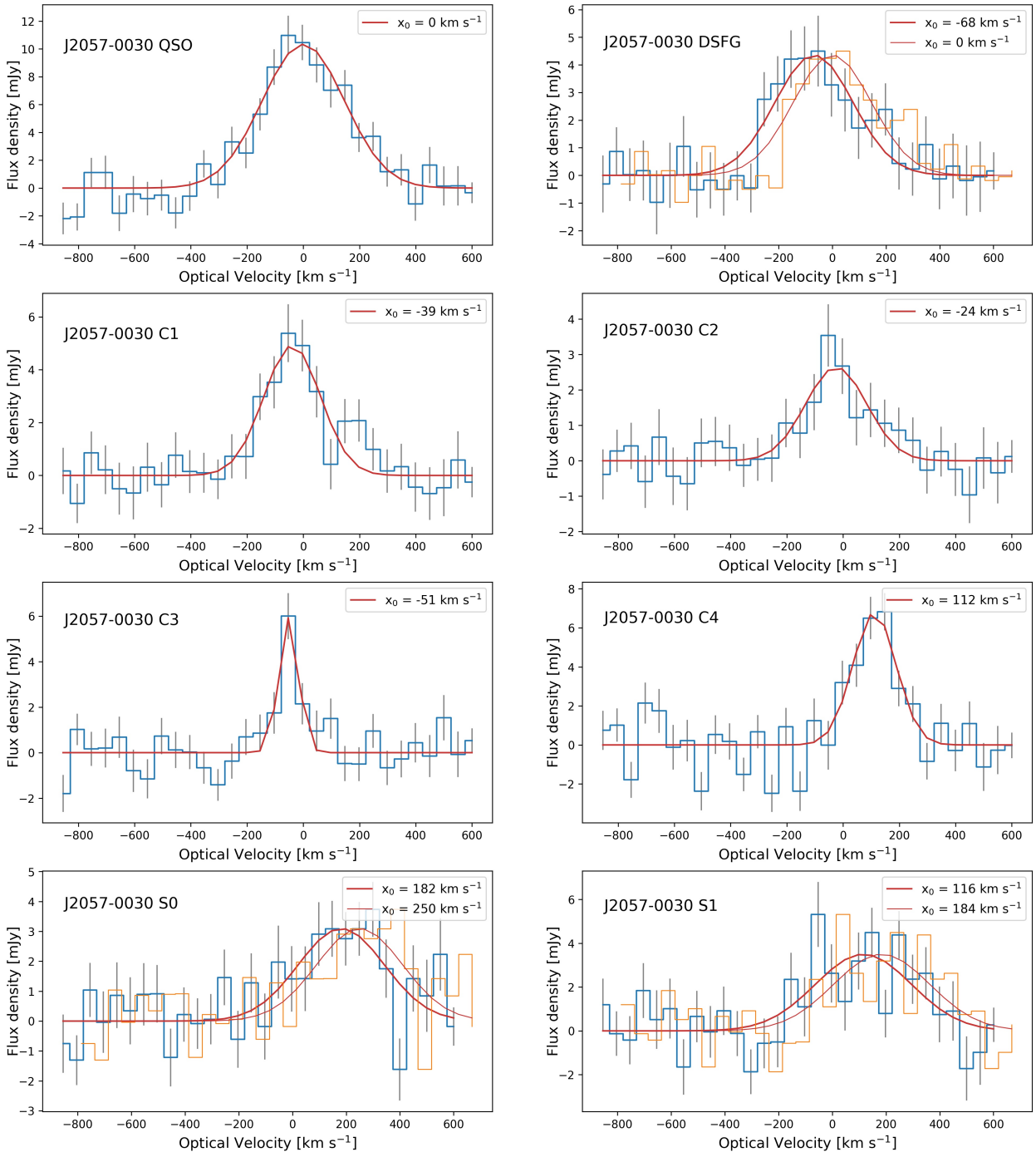

Figure 3.2: Spectra of the [CII] λ157.74 μm emission line for all the components of the system. A 1D Gaussian fit is shown as a solid red line with its respective center x_0 shown in the right corner. The orange line represents the spectra of the sources centered at the x_0 of the DSFG. The rms is plotted as gray bars.

Table 3.1: Spectral measurements

Component	Cont. Flux [mJy]	ν [GHz]	Cont. Size [″]	$F_{[CII]}$ [Jy km s^{-1}]	$FWHM_{[CII]}$ [km s^{-1}]	$\nu_{0,[CII]}$ [GHz]	[CII] Size [″]	$L_{[CII]}$ [10^9 $L_\odot$]	Δd [kpc]	Δv [km s^{-1}]
QSO	2.44 ± 0.24	346.52	0.76 ± 0.04 × 0.68 ± 0.03	3.79 ± 0.24	344.9 ± 49.6	334.45	1.14 ± 0.05 × 0.92 ± 0.05	2.59 ± 0.16	...	...
DSFG	1.48 ± 0.33	346.52	1.48 ± 0.3 × 1.0 ± 0.2	1.58 ± 0.22	342.6 ± 68.8	334.53	1.28 ± 0.13 × 0.34 ± 0.03	1.08 ± 0.15	19.4	-68.1
C1[a,b]	0.29 ± 0.22	346.52	< 0.64 × 0.58	1.24 ± 0.16	238.2 ± 51.8	334.5	< 0.64 × 0.58	0.85 ± 0.11	4.5	-39.5
C2[a,b]	0.23 ± 0.18	346.52	< 0.82 × 0.76	0.72 ± 0.13	256.7 ± 70.2	334.48	< 0.82 × 0.76	0.49 ± 0.09	8.5	-24.5
C3[a,b]	0.49 ± 0.21	346.52	< 1.01 × 0.82	0.52 ± 0.1	81.8 ± 24.4	334.51	< 1.01 × 0.82	0.35 ± 0.07	11.4	-51.3
C4[b]	0.38 ± 0.25	346.52	< 0.88 × 0.74	1.3 ± 0.16	180.8 ± 58.2	334.33	0.88 ± 0.09 × 0.74 ± 0.07	0.89 ± 0.11	27.8	111.9
S0[b,c]	0.52 ± 0.25	346.52	< 0.92 × 0.68	1.24 ± 0.22	378.6 ± 148.0	334.34	0.92 ± 0.14 × 0.68 ± 0.1	0.85 ± 0.15	5.8	249.7
S1[b,c]	0.04 ± 0.3	346.52	< 1.32 × 0.88	1.57 ± 0.28	421.8 ± 182.8	334.42	1.32 ± 0.26 × 0.88 ± 0.18	1.07 ± 0.15	10.2	184.0

Note. Columns: (1) Component; (2) Continuum fluxes (in mJy); (3) Continuum frequency (in GHz); (4) Beam deconvolved sizes of the continuum emitting region (in arcseconds); (5) [CII] integrated fluxes (in Jy km s^{-1}); (7) Full width at half maximum (FWHM) of the Gaussian fit of the [CII] 1D spectra (in km s^{-1}); (8) Observed central frequency of the [CII] line (in GHz); (9) Beam deconvolved sizes of the [CII] emitting region (in arcseconds); (10) [CII] luminosities (in $L_\odot$); (11) Distances between the sources and the QSO host, calculated assuming the redshifts of the quasar hosts' [CII] emission lines (in kpc); (12) Velocity offsets with respect to the QSO host, calculated from the central frequencies of the [CII] emission lines (in km s^{-1}).

[a] [CII] unresolved sources, sizes have upper limits only.

[b] Continuum unresolved sources, sizes have upper limits only.

[c] Distances in column (11) are measured relative to the DSFG.

Table 3.2: Redshifts

Component	$z_{\rm CII}$	$z_{\rm SDSS}$	$\Delta v_{\rm SDSS}$ km s^{-1}	$z_{\rm MgII}$	$\Delta v_{\rm MgII}$ km s^{-1}
QSO	4.683	4.663	+1064	4.680	+158

Note. Columns: (1) Component; (2) [CII]-based redshift; (3) SDSS-based redshift taken from Hewett & Wild (2010); (4) SDSS redshift offset with respect to the [CII] redshift; (5) MgII λ2798-based redshifts taken from Trakhtenbrot et al. (2011); (6) MgII redshift offset with respect to the [CII] redshift.

3.1.1. [CII] velocity offsets

The low ionization MgII $\lambda \sim 2798$ $\AA$ line (15.04 eV) is produced in the broad line region (BLR) of the AGN of galaxies and its average velocity has been observed to be closer to the systemic velocity of the quasar (e.g., Hewett & Wild, 2010). For this reason, it is commonly used to determine the systemic redshifts (z) of quasars but as its emission is broad, the uncertainty in the line center is expected to be large. In N20, the redshift of the quasar is reported based on the best model fit to the MgII emission line and it is compared to an estimation using [CII] as it is expected that this line is a good tracer of low ionization gas in the interstellar medium of the quasar host. The results did not match and noticeable blueshifts were found not only in this object but as a common characteristic of high-z quasars (N20). We repeat the procedure in order to compare our estimation of the redshift of J205724.14 to that reported in N20, as our data have no gap in the [CII] spectrum. The results were identical to those of N20 with an estimated redshift $z \sim 4.683$ for the galaxy host, implying that the Gaussian fit in N20 was not affected by the missing channels.

In Table 3.2 we compare the redshift obtained from the [CII] and MgII lines of the quasar host, including the SDSS-based redshift determinations published in Hewett & Wild (2010) for comparison. The difference between the redshift determinations of SDSS compare to [CII] ($\Delta v_{\rm SDSS}$) is large but the uncertainties in z_{SDSS} are also significant as the SDSS determination of the redshift is based on UV emission lines which are known for being problematic (e.g., [C$_{\rm IV}$] often showing asymmetries and significant blueshifts). As already mentioned, in N20 a compilation of sources from other works at $z \gtrsim 5$ was done (see N20 and references therein) to determine a mean value of the MgII velocity offset, resulting in $z_{\rm CII} - z_{\rm MgII} = 372 \pm 582$ km s^{-1}. These uncertainties in the velocity shift are not expected to be related to the fitting of the broad emission line, with works as Shen et al. (2016) reporting an intrinsic uncertainty of ~ 200 km s^{-1} only. The $\Delta v_{\rm MgII}$ for our QSO is ~ 158 km s^{-1}, which is smaller than the mean value of N20 compilation. For the DSFG, we determine a $z_{\rm CII} \approx 4.681$.

It is worth mentioning that N20 suggested a possible link between merger activity and a small velocity shift $\Delta v_{\rm MgII}$ based on the sources from Decarli et al. (2018), where 2/4 quasars with companions have tabulated [CII]-MgII offsets yielding a mean velocity offset of ~ 0 km s^{-1} (see Table 6 of N20). This idea is primarily speculative until more sources with companions are included in the study.

3.1.2. [CII] moments

Figure 3.3 displays the moment 0 map of the system, where we can observe the spatial distribution of the components as seen at two different resolutions. On the left panel of the plot we show the moment 0 for the low spatial resolution data with black solid (dashed) contours indicate the positive (negative) significance levels at [2, 2.5, 3, 3.5, 4, 5, 8]σ of [CII] flux, where $\sigma_{[CII]} = 0.218$ Jy km s^{-1} beam^{-1}. All the components of the system are described in Section 2.4. On the right panel we show the moment 0 map for the high spatial resolution data with $\sigma_{[CII]} = 0.046$ Jy km s^{-1} beam^{-1}, where we can see some complex structures specifically towards the north and to the south-west at lower brightness levels, implying that we may be starting to resolve the QSO host. The same occurs at the position of the DSFG. This result encourages the pursuit of higher resolution and deeper observations for this system. The rest of the components are seen as faint sources, not very distinguishable from the background.

To calculate moment 1 and 2 of the QSO and the neighbouring clumps (C1, C2, C3 and C4), we used the [CII] emission cubes at a rest frame frequency equal to the center of the 1D Gaussian fit applied to the QSO spectra, this is $\nu_{0,[CII]} \sim 334.45$ GHz. We did the same with the DSFG and the clumps S0 and S1, setting the rest frame frequency equal to the center of the 1D Gaussian fit of the DSFG spectra, $\nu_{0,[CII]} \sim 334.53$ GHz, in order to differentiate the moments as the DSFG shows a velocity offset of $\sim$ -68 km s^{-1} from the quasar. We did not apply any mask at the time of the creation of these moments but we showed them in Figure 3.4 and 3.5 using a mask based on the moment 0 map, showing the emission with a significance level $\geq 2\sigma$.

Figure 3.4 left panel shows the velocity fields map for the QSO host and neighbouring clumps. The main source has a marked velocity gradient along the east–west axis, that ranges from $\sim$ -80 km s^{-1} for the east region of the host to $\sim$ +50 km s^{-1} in the west side of the QSO, apparently representing a rotating disk with an "S" pattern in the center of the galaxy which is likely not significant as the region has a size comparable to the synthesized beam. The right panel of Figure 3.4 shows the velocity dispersion map, where the QSO shows a strong dispersion in the northern region, exhibiting velocity dispersions of about $\sim$ 180 km s^{-1}. While these could be due to ongoing physical processes with the current data we cannot rule out that this pattern may be produced by noise effects due to the low signal-to-noise ratio (S/N) in the border of the host. In the case of the Southern region of the galaxy, a velocity dispersion of about $\sim$ 120 km s^{-1} is displayed and seems to be a more trustful result than its counterpart as it extends further from the limits of the host to the center region. For C1, C2 and C3 it is not feasible to derive any conclusion about the gradients exhibited in both velocity maps as their sizes are comparable to the beam size.

Figure 3.5 left panel shows the velocity fields map for the DSFG and its clumps, S0 and S1. The galaxy exhibits a velocity gradient that ranges from $\sim$ -50 km s^{-1} for the south-east side to $\sim$ +80 km s^{-1} in the west region of the DSFG, suggesting the presence of a rotational disk in the DSFG. The S0 clump seems to have a rather homogeneous velocity of $\sim$ +100 km s^{-1} with respect to the systemic velocity of the DSFG, a value similar to the velocity observed on the west side of the DSFG. Found at a separation of $\sim$ 6 kpc, this suggests that

S0 and the DSFG are physically connected. In the case of S1 a higher and again almost homogeneous velocity of $\sim +150$ km s^{-1} is observed. In the left panel of Figure 3.5 we can see that the velocity dispersion is very high for both S0 and S1. If they are real, they could be interpreted as objects supported by dispersion. However, since both clumps are barely resolved this result is only speculative.

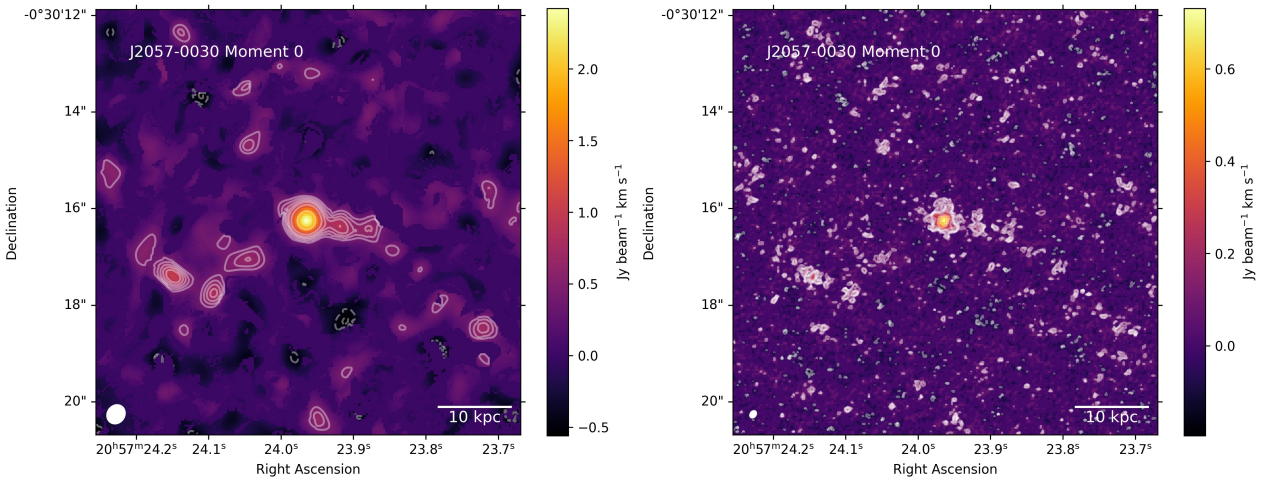

Figure 3.3: Integrated value of the [CII] spectrum map (moment 0) as seen with two different beam sizes. Left: the beam size is $0.41'' \times 0.36$ at P.A = -35.69°. Right: the beam size is $0.16'' \times 0.12''$ at P.A = -35.69°. White solid (dashed) contours indicate the positive (negative) significance levels at [2, 2.5, 3, 3.5, 4, 5, 8] σ. The synthesized beam is shown at the bottom-left corner as a white filled ellipse. North is up and east is to the left.

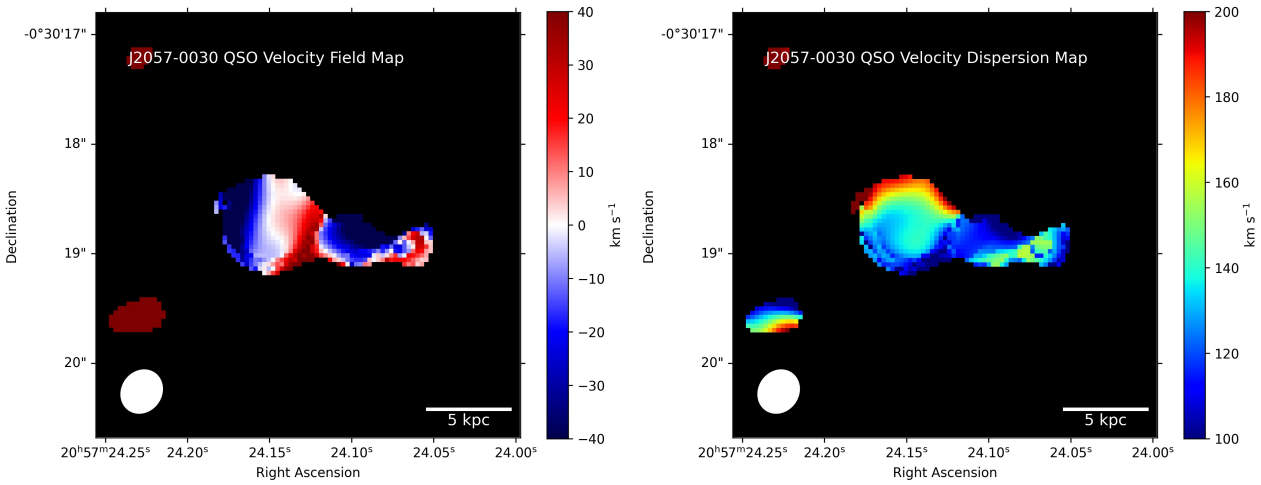

Figure 3.4: Velocity fields map (moment 1) and velocity dispersion map (moment 2) of the Quasar (QSO) and its clumps (C1, C2, C3). The synthesized beam is shown at the bottom-left corner as a white filled ellipse. North is up and east is to the left.

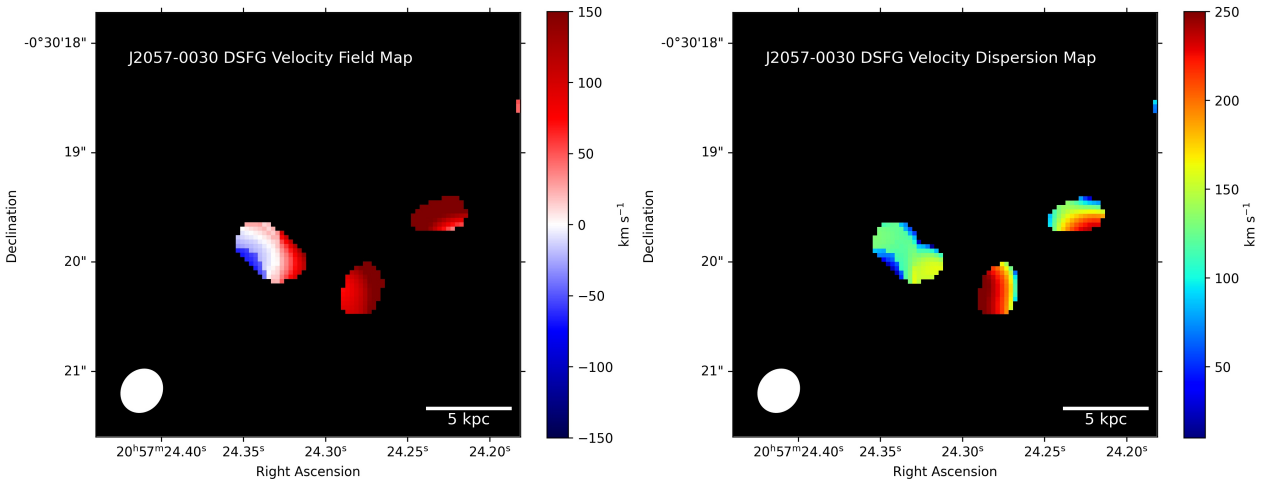

Figure 3.5: Velocity fields map (moment 1) and velocity dispersion map (moment 2) of the dusty star-forming galaxy (DSFG) and its clumps (S0 and S1). The synthesized beam is shown at the bottom-left corner as a white filled ellipse. North is up and east is to the left.

3.2. Dust emission properties

3.2.1. SED and SFRs

Using the rest frame FIR continuum emission we estimate the total IR emission of our objects. Since the J205724.14 system only has two ALMA detections, both at ~ 152 μm, it is not possible to model the spectral energy distribution (SED) based on this single point. Instead, we can estimate which SED model can represent our observations. We assume that in all of our objects the FIR emission is dominated by dust heated through star formation (SF) and then we disregard the AGN contribution to the SEDs as it should be as low as $\sim$ 10%, based on several studies of the mid-to-far IR SEDs of luminous AGN (e.g., Schweitzer et al., 2006; Mor & Netzer, 2012; Rosario et al., 2012; Lutz et al., 2016).

We consider an additional uncertainty based on ALMA absolute flux calibration in band-7 of the order of 10% according to ALMA Cycle 6 Technical Handbook and we add this in quadrature to the flux measurement errors. We suggest treating this 10% contribution with caution as it has been a debated value, with works as Francis et al. (2020) arguing that the calibration can be poorer than the nominal number and can be affected by weather-related phase decorrelation when self-calibration of the science target is either not possible or not attempted.

For the model, we choose a modified black-body SED to fit the quasar host and the dusty star-forming galaxy IR emission using 3 different temperatures based on two different works. First, from Sommovigo et al. (2022) the range of dust temperatures at $z \sim 5$ goes from $\sim$ 35 K to 60 K for objects with luminosities of the order of 10^{11} $L_{\odot}$ and star formation rates (SFR) of a few tens of $M_{\odot}$ yr^{-1}. This is about one order of magnitude smaller than the luminosities and SFRs of the sources analyzed by N20, including those in the J205724.14

system. Based on this, we consider the objects in Sommovigo et al. (2022) to be representative of a less luminous group of galaxies. Therefore we assume that our objects should exhibit temperatures in a range that goes from the temperatures of these sources to greater values. Thus, we select T = 40 K as the lower limit for the temperature.

For the upper limit, we analyzed the 9 FIR-bright sources of N20, where FIR-Bright refers to objects that have been detected by Herschel/SPIRE instruments and represent a more luminous population of objects ($L_{\rm FIR} \sim 10^{13}\ L_{\odot}$) than the FIR-Faint sources which were not detected by Herschel/SPIRE. Using these 9 bright objects they determined the best gray-body SEDs that fit the 3 Herschel/SPIRE measurements at 250, 350 and 500 μm and the ALMA observations using a wide range of temperatures T = [40, 45, 50, 55, 60 and 70] K and emissivity coefficients β = 1.5 and 1.7. The results can be seen in Figure 7 of N20 from which they concluded that 7/9 objects are well fit by temperatures from 40 K to 50 K. Based on this result, we choose a T = 50 K as the upper limit for the temperature. We set an intermediate temperature as the median value of the first two, that is T = 45 K and an emissivity coefficient $\beta = 1.6$ (e.g., Beelen et al., 2006; Trakhtenbrot et al., 2017, N20).

The SED for each component of our system is shown in Figure 3.6, where the blue line shows the SED at T = 40 K, the green one at T = 45 K and the red line at T = 50 K. The QSO and the DSFG are the only sources that we considered to have a real detection of the continuum. Meanwhile, all the clumps will be treated as upper limits for the measured continuum emission. Typically, DSFGs have lower dust temperatures compared to QSOs, however, we chose to work with the same temperatures for both sources as we consider that the range selected for the SEDs is wide enough to account for these differences in T. We estimated the total FIR luminosity ($L_{\rm FIR}$) by integrating the resulting SEDs over the 8-1000 μm range. The $L_{\rm FIR}$ of the QSO and the DSFG at T = 45 K is in good agreement with the FIR luminosities reported in N20 for SEDs with T = 47 K and $\beta = 1.6$.

The SFRs were obtained from these FIR luminosities using Equation 3.1 from Kennicutt (1998) after assuming a Chabrier initial mass function (IMF) from Chabrier (2003) (as adopted by Nordon et al. (2012)). The SFRs range goes from a few dozen $M_{\odot}$ yr^{-1} in the case of the upper limits determined for the clumps to a few hundred $M_{\odot}$ yr^{-1} in the case of the QSO host and the DSFG (see Table 3.3). For the DSFG we see a slight increment in the SFR from the value reported in N20 of 100 $M_{\odot}$ yr^{-1}. However, the regions in which the continuum flux was measured are quite different. In N20 two components were found for the DSFG, both with sizes smaller than 0.3″ and only one of them was used to calculate the SFR, meanwhile, we use an estimated size of 1.48″×1″.

$$\frac{\rm SFR}{\rm M_{\odot}\ yr^{-1}} = \frac{1.1 \cdot L_{\rm IR}}{10^{10} L_{\odot}} \tag{3.1}$$

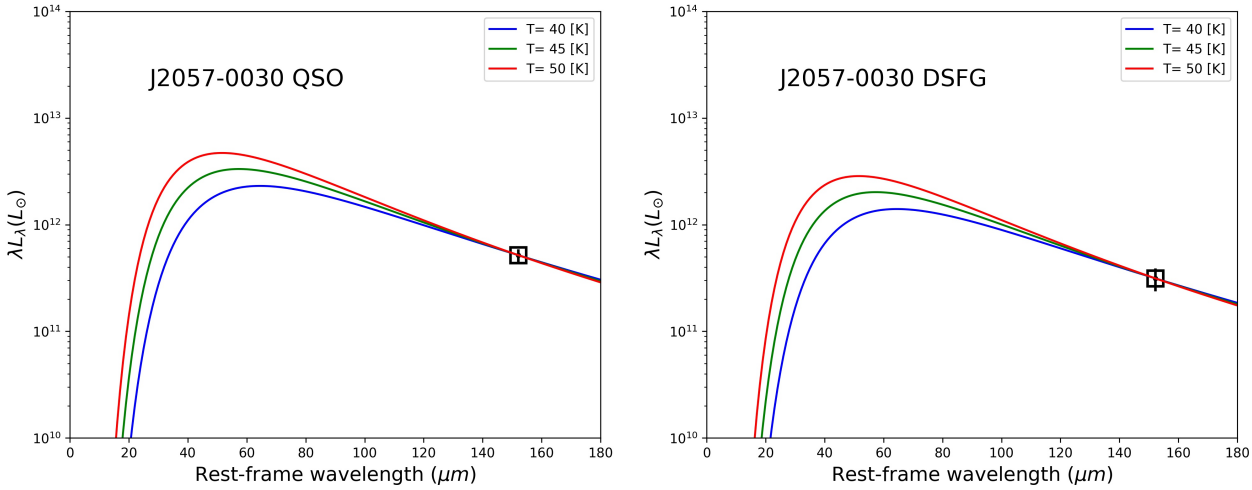

Figure 3.6: FIR SEDs for the quasar and the dusty star-forming galaxy (DSFG) using an emissivity coefficient $\beta = 1.5$ with 3 different temperatures = (40, 45, 50) K represented by the solid blue, green and red lines, respectively. The data point corresponds to ALMA detection at 895 μm (in the observed frame).

Table 3.3: Galaxy properties: FIR luminosity and SFR.

Component	log L_{40K} $[L_\odot]$	log L_{45K} $[L_\odot]$	log L_{50K} $[L_\odot]$	SFR_{40K} $[M_\odot\ yr^{-1}]$	SFR_{45K} $[M_\odot\ yr^{-1}]$	SFR_{50K} $[M_\odot\ yr^{-1}]$
QSO	12.4 ± 0.06	12.56 ± 0.06	12.71 ± 0.06	279 ± 35	402 ± 51	568 ± 72
DSFG	12.19 ± 0.11	12.35 ± 0.11	12.5 ± 0.11	169 ± 38	244 ± 38	345 ± 38
C1*	11.48 ± 0.33	11.64 ± 0.33	11.79 ± 0.33	33 ± 23	48 ± 23	68 ± 23
C2*	11.38 ± 0.34	11.54 ± 0.34	11.69 ± 0.34	27 ± 19	38 ± 19	54 ± 19
C3*	11.71 ± 0.19	11.87 ± 0.19	12.02 ± 0.19	56 ± 22	81 ± 22	114 ± 22
C4*	11.59 ± 0.3	11.75 ± 0.3	11.9 ± 0.3	43 ± 27	62 ± 27	88 ± 27

Note. Columns: (1) Component; (2), (3), (4) FIR luminosities (in $L_\odot$) calculated by integrating from 8 to 1000 μm the SEDs constructed with $\beta = 1.6$ and T = 40 K, 45 K and 50 K, respectively; (5), (6), (7) star formation rates (SFRs, in $M_\odot\ yr^{-1}$) estimated using Equation 3.1 with L_{40K}, L_{45K} and L_{50K}, respectively. Asterisks (*) represent upper limits only.

3.3. L_{CII}/L_{FIR} versus L_{FIR}

The L_{CII}/L_{FIR} ratio is a measure of the amount of cooling due to gas and dust emission in star-forming galaxies. Main sequence (MS) galaxies tend to follow a constant relation, with [CII] luminosities scaling linearly with IR luminosities, although the correlation has a significant scatter. However, when high-IR luminosity sources, as local (U)LIRGs ($L_{IR} \geq 10^{12}\ L_\odot$), are analyzed, a decrease in the L_{CII}/L_{FIR} ratio is found, with [CII] being deficient with respect to the IR luminosity. This is also observed in high-z sources (Malhotra et al., 1997; Díaz-Santos et al., 2013; Magdis et al., 2014; Díaz-Santos et al., 2017).

Figure 3.7 shows the L_{CII} - L_{FIR} relation as a solid black line as estimated by Magdis et al. (2014) for local normal galaxies from Malhotra et al. (2001), which implies a constant

$L_{\rm CII}/L_{\rm FIR}$ ratio. The dashed lines represent the scatter in the relation of 0.3 dex. J205724.14 components are plotted: QSO (red circle), the DSFG (green star) and the clumps C1, C2, C3 and C4 (as a cyan triangle-up, a yellow triangle-down, a pink triangle-right and a blue triangle-left, respectively). These points are calculated using the $L_{\rm FIR}$ obtained after integrating the SEDs constructed with T = 45 K and β = 1.6. The error bars symbolize the uncertainty associated with the aperture measurement of the [CII] and FIR emission. For the clumps, only upper limits of the $L_{\rm FIR}$ are shown. For comparison, local LIRGS from Díaz-Santos et al. (2017) are plotted as grey dots. High-z sources are plotted with orange symbols. The plus symbols represent SF galaxies from Decarli et al. (2018), the squares are galaxies classified as SF and AGN from Stacey et al. (2010), and the crosses represent the sample from N20. The measurements for the J205724.14 QSO host and the DSFG done by N20 are also included using a purple circle and a purple star, respectively. The QSO host and the DSFG are displaced from the relation with a lower $L_{\rm CII}$ than expected compared to their FIR luminosities. This means that at least our main components are clearly [CII] deficient. The higher the $L_{\rm FIR}$ of a galaxy, the more it displaces from the relation (Magdis et al., 2014).

Another common way to illustrate this relationship is to plot the [CII] to FIR continuum luminosity ratio as a function of $L_{\rm FIR}$ as in Figure 3.8, where our sources are represented using the same symbols as in Figure 3.7. As the clumps have only upper limits of the $L_{\rm FIR}$, only lower limits for the $L_{\rm CII}/L_{\rm FIR}$ ratio are shown. In panel (a), the error bars symbolize the uncertainty associated with the aperture measurement of the [CII] and FIR emission. In panel (b), the bars represent the $L_{\rm FIR}$ and $L_{\rm CII}/L_{\rm FIR}$ ratio obtained using the FIR luminosity when the SEDs are constructed with temperatures T = 40 K (blue bar) and T = 50 K (red bar). Lastly, in panel (c) the bars represent the quadratic sum of the uncertainties in the measurement of the FIR emission while using T = 45 K as in (a) and the values for the $L_{\rm FIR}$ and $L_{\rm CII}/L_{\rm FIR}$ ratio using T = 40 K and T = 50 K as in (b). From the quadratic sum, it is straightforward to see that when modeling the SEDs the uncertainties in the $L_{\rm CII}/L_{\rm FIR}$ ratio are dominated by the uncertainties in the measurements of $L_{\rm CII}$ and $L_{\rm FIR}$ instead of the assumed temperature. These plots clearly demonstrate that the $L_{\rm CII}/L_{\rm FIR}$ ratio is not a constant value, but a strong function of $L_{\rm FIR}$, although with large scatter.

Typical $\log(L_{\rm CII}/L_{\rm FIR})$ values for local star-forming galaxies go from $\sim$ -2.5 to $\sim$ -2. In contrast, local (U)LIRGs can decrease about one order of magnitude, having ratios similar to high-z star-forming galaxies with $\log(L_{\rm CII}/L_{\rm FIR})$ in the range $\sim$ (-3.5, -2.5). For high-z sources with FIR luminosities higher than 10^{12} $L_{\odot}$ the deficit is very prominent with values of $\log(L_{\rm CII}/L_{\rm FIR}) <$ -3.5 (Farrah et al., 2013; Díaz-Santos et al., 2013, 2017; Decarli et al., 2018), including several of the sources published by N20. The sources observed by Stacey et al. (2010) seem to define a new high-z sequence, parallel to the one observed for other sources.

The lower limits calculated for the clumps C1, C2, C3 and C4 show $\log(L_{\rm CII}/L_{\rm FIR})$ ratios in the range between -3.3, -2.8, closer to local LIRGs ratios (e.g., Díaz-Santos et al., 2017). This result is expected as these components show the lowest FIR continuum emission. In contrast, the QSO host and the DSFG have $\log(L_{\rm CII}/L_{\rm FIR})$ ratios of -3.2 and -3.3, respectively. These values are comparable to high-redshift star-forming galaxies as those from Decarli et al. (2018). From Figure 3.7 and 3.8, it is evident that our sources are [CII] deficient with respect

to their FIR luminosity, as observed in local (U)LIRGs with respect to local main sequence galaxies.

The physical origin of the [CII] deficit remains unsolved. However, different explanations have been proposed, including reduced photoelectric heating caused by positively-charged dust grains and absorption of ionizing and UV photons by dust in HII regions (see Casey et al., 2014), optically thick [CII] emission, the influence of the AGN activity (Smith et al., 2017), the low metallicity in galaxies (Vallini et al., 2015), or the [CII] saturation at high temperatures (e.g., Díaz-Santos et al., 2013; Gullberg et al., 2015). Whichever of these processes is involved, it seems that the deficit is restricted to the nuclear region of galaxies, where the starburst is ongoing (Díaz-Santos et al., 2014; Smith et al., 2017). It is important to note that this [CII] deficit at high luminosities is also reported for other lines such as [O_I], [O_{III}], [N_{II}] and [N_{III}] indicating that it represents a general effect of all FIR fine structure lines, regardless if they arise from the ionized or neutral phase of the ISM (Graciá-Carpio et al., 2011; Farrah et al., 2013; Díaz-Santos et al., 2017).

Notice should be taken that the FIR luminosities of our sources were obtained after integrating the SED constructed at a fixed temperature (T = 45 K). Then a direct connection between our selection of T with the deficit is expected as low and high-z sources show an increment in the [CII] deficit at higher temperatures (Díaz-Santos et al., 2017). However, we have seen that the $L_{\rm CII}/L_{\rm FIR}$ ratio did not change drastically when we made the SEDs using T = 40 K and T = 50 K so we can argue that the contribution of our selection of a dust temperature is probably not significant in the [CII] deficit observed in our sources except if we are substantially under(over) estimating the constraints in the temperatures. This is likely not the case unless our sources were particularly rare and not comparable to the ones in Sommovigo et al. (2022) (from which we take T = 40 K) and the FIR-Bright sources of N20 (from which we take T = 50 K).

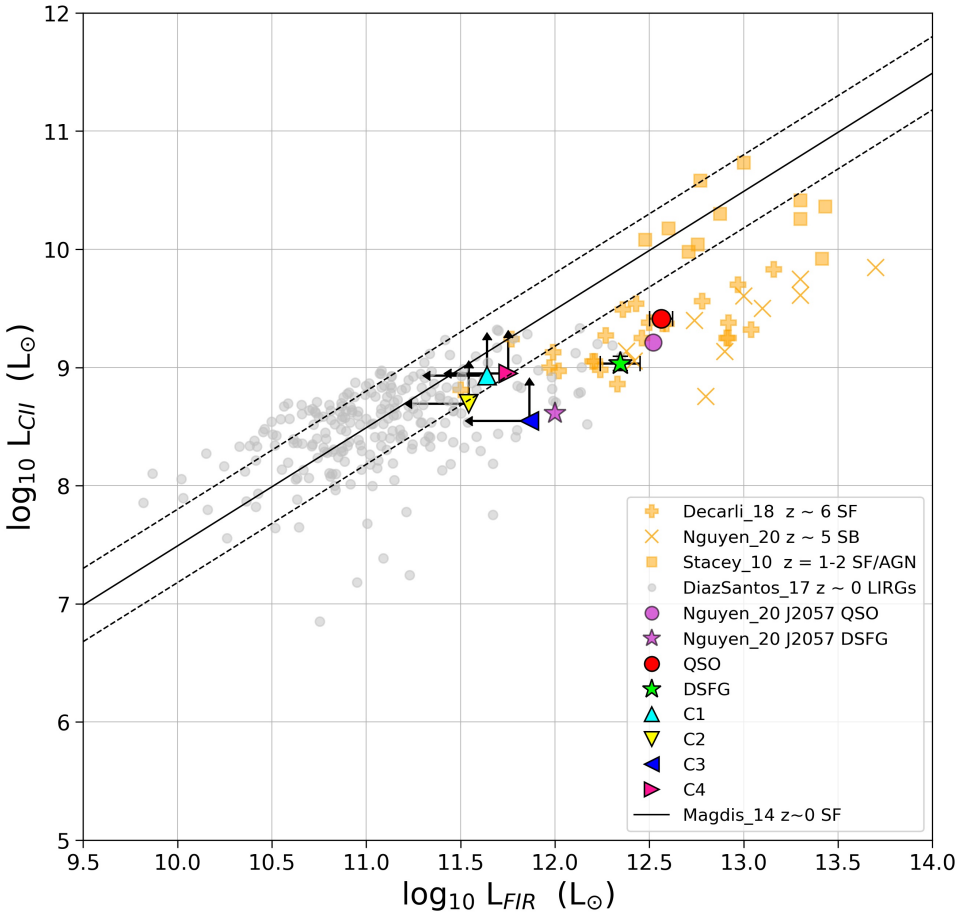

Figure 3.7: $L_{\rm CII}$ vs $L_{\rm FIR}$. The sources are plotted as a red circle for the QSO and a green star for the DSFG. The clumps C1, C2, C3 and C4 are plotted as a cyan triangle-up, a yellow triangle-down, a pink triangle-right and a blue triangle-left, respectively. The FIR luminosities are obtained by integrating from 8 to 1000 μm the SEDs constructed with T = 45 K and $\beta = 1.6$. The error bars symbolize the uncertainty associated with the aperture measurement of the [CII] and FIR emission. For the clumps, only upper limits of the $L_{\rm FIR}$ are reported. The solid black line represents the best linear fit found by Magdis et al. (2014) for the local normal galaxies from Malhotra et al. (2001). The dashed lines represent the scatter of the relation of 0.3 dex.

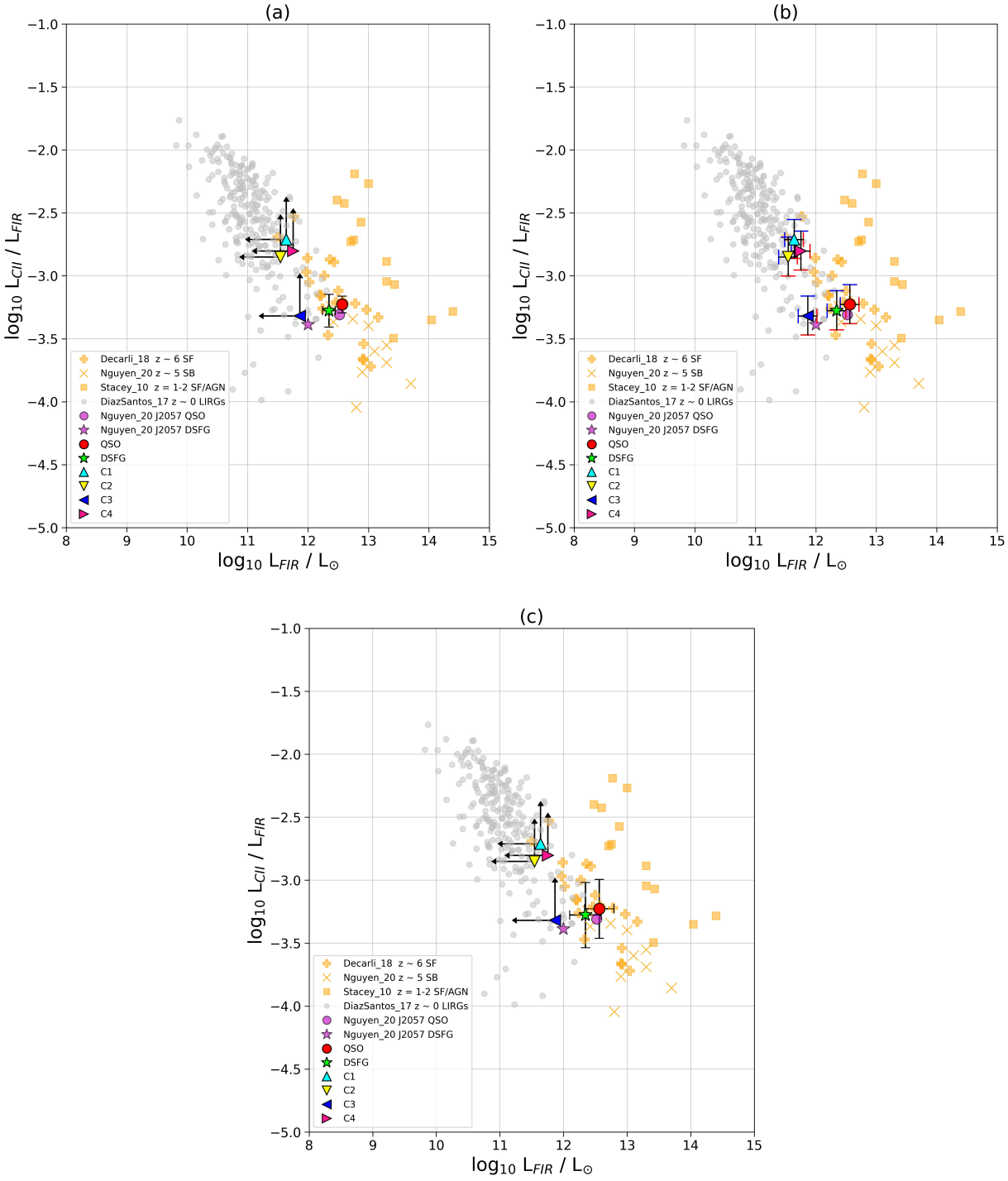

Figure 3.8: $L_{\rm CII}/L_{\rm FIR}$ ratio vs $L_{\rm FIR}$. The sources are plotted as a red circle for the QSO and a green star for the DSFG. The clumps C1, C2, C3 and C4 are plotted as a cyan triangle-up, a yellow triangle-down, a pink triangle-right and a blue triangle-left, respectively. The FIR luminosities are obtained by integrating from 8 to 1000 μm the SEDs constructed with T = 45 K and $\beta = 1.6$. For the clumps upper limits of the $L_{\rm FIR}$ are reported, yielding only lower limits for the $L_{\rm CII}/L_{\rm FIR}$ ratio. In panel (a) the error bars symbolize the uncertainty associated with the aperture measurement of the [CII] and FIR emission. In panel (b), the bars represent the $L_{\rm FIR}$ and $L_{\rm CII}/L_{\rm FIR}$ ratio obtained using the FIR luminosity when the SEDs are constructed with temperatures T = 40 K (blue bar) and T = 50 K (red bar). In panel (c) the bars represent the quadratic sum of the uncertainties in (a) and (b).

Chapter 4

Dynamical, dust and gas masses

In this chapter, we derive the properties of the sources such as their dust, gas, and dynamical masses based on several assumptions. We note, however, that the uncertainties associated to these measurements are large and for this reason, we suggest treating the following discussions with caution.

4.1. Dynamical masses $M_{\rm dyn}$

We estimate the dynamical masses ($M_{\rm dyn}$) for the quasar host and the DSFG using the [CII] line, assuming that the [CII]-traced interstellar medium (ISM) is distributed in an inclined, rotating disk (see Wang et al., 2013; Willott et al., 2015; Venemans et al., 2016), following:

$$M_{\rm dyn} = 9.8 \times 10^8 \left(\frac{D_{\rm [CII]}}{\rm kpc}\right) \left[\frac{\rm FWHM[CII]}{100\ \rm kms^{-1}}\right]^2 \frac{1}{\sin^2(i)} M_\odot \tag{4.1}$$

Where $D_{\rm [CII]}$ is the size of the [CII] emitting region measured by the deconvolved major axis of the Gaussian fit. The term $\sin(i)$ represents the inclination angle between the line of sight and the polar axis of the host gas disks, with the circular velocity given as $v_{circ} = 0.75 \times$ FWHM/$\sin(i)$. Assuming a thin-disk geometry, we can determine the inclination of the disk (i) following $\cos(\rm i) = a_{\rm min}/a_{\rm maj}$, where $a_{\rm min}$, $a_{\rm maj}$ are the semi-minor and semi-major axes of the [CII] emitting regions, respectively. The uncertainties for this method are large, especially caused by the uncertainties in the major and minor axis of the [CII] emitting region which is used to estimate $\rm D_{[CII]}$ and i. The dynamical masses $M_{\rm dyn}$ of our sources are reported in Table 4.1, where we have included the inclination uncorrected $M_{\rm dyn}^{\rm uncorr}$ (i.e., $M_{\rm dyn}^{\rm uncorr} = M_{\rm dyn} \times \sin^2(\rm i)$). For the QSO host $M_{\rm dyn}$ is $10^{11.4\pm0.1}$ $M_\odot$ and $M_{\rm dyn}^{\rm uncorr} \sim 10^{10.9\pm0.1}$ $M_\odot$. For the DSFG $M_{\rm dyn}$ and $M_{\rm dyn}^{\rm uncorr}$ are $\sim 10^{11\pm0.1}$ $M_\odot$.

If we follow the assumption that our galaxies are not supported by rotation but instead, are

dominated by dispersion Decarli et al. (2018), we can estimate the dispersion mass ($M_{\rm disp}$) using Equation 4.2 derived from the Virial theorem:

$$M_{\rm disp} = \frac{3}{2}\frac{a_{\rm maj}\sigma^2_{\rm line}}{G} \tag{4.2}$$

Where $a_{\rm maj}$ is the major axis of the [CII] region, $\sigma_{\rm line}$ is the line width of the Gaussian fit of the [CII] spectrum and G is the gravitational constant. These dispersion masses $M_{\rm disp}$ are $\sim 10^{10.5\pm0.1}$ $M_\odot$ for the QSO host and the DSFG (see Table 4.1).

The values reported here for the quasar host are larger than those calculated by N20 for the $M_{\rm dyn}$, $M^{\rm uncorr}_{\rm dyn}$ and $M_{\rm disp}$ by 0.4, 0.7 and 0.2 dex, respectively. The increases in the dynamical and dispersion masses of the QSO are correlated with the [CII] size measured with Cycle 6, $1.14'' \times 0.92''$ compared to a N20 size of $0.4'' \times 0.18''$. For the $M^{\rm uncorr}_{\rm dyn}$ the difference is mainly due to our larger estimate of the FWHM ~ 345 km s^{-1} compared to a FWHM $\sim$ 331.4 km s^{-1} in N20. For the DSFG we see that the $M_{\rm dyn}$ and $M^{\rm uncorr}_{\rm dyn}$ are consistent with our values. In the case of $M_{\rm disp}$ we see a smaller value than N20 by 0.3 dex. This happens because even though we obtained a larger size for the DSFG than N20, the FWHM measurement, with a big impact on the calculations, is ~ 347 km s^{-1}, while N20 estimated for the region that contains both of the components of the DSFG a FWHM ~ 512 km s^{-1} yielding larger value for $M_{\rm disp}$.

The uncertainties in the masses of about 0.1 dex are rather smaller considering the number of assumptions in their estimations. However, we must notice that they include only the formal errors and they do not take into account the uncertainties in the selection of a model to describe the kinematics of the system, which are expected to be large based on how different the values of the dynamical masses are when we assume a disk model ($M_{\rm dyn}$) compared to a bulge model ($M_{\rm disp}$).

4.2. Dust masses $M_{\rm dust}$

The continuum emission at rest wavelength $\lambda \sim 152$ μm can be used to calculate the dust masses ($M_{\rm dust}$) of our main source and its companion assuming that the FIR continuum flux originates from optically thin dust at these wavelengths (Dunne et al., 2000; Beelen et al., 2006) using Equation 4.3:

$$M_{\rm dust} = \frac{S_\lambda(\lambda_{\rm rest})D_L^2}{\kappa_d(\lambda_{\rm rest})B_\lambda(\lambda_{\rm rest}, T_d)} \tag{4.3}$$

Where $S_\lambda(\lambda_{\rm rest})$ is the continuum flux density at $\lambda_{\rm rest}$, D_L is the luminosity distance, $\kappa_d(\lambda_{\rm rest})$ is the wavelength dependent dust mass opacity and $B_\lambda(\lambda_{\rm rest}, T_d)$ is the monochromatic value of the Planck function at $\lambda_{\rm rest}$ for the dust temperature T_d. Dunne et al. (2000) found that

Table 4.1: Galaxy properties: masses.

Component	log $M_{\rm dyn}^{\rm uncorr}$ $[M_\odot]$	log $M_{\rm dyn}$ $[M_\odot]$	log $M_{\rm disp}$ $[M_\odot]$	log $M_{\rm dust}$ $[M_\odot]$	log $M_{\rm gas}$ $[M_\odot]$	log $M_{\rm mol}$ $[M_\odot]$
QSO Host	10.9 ± 0.1	11.4 ± 0.1	10.5 ± 0.1	8.5 ± 0.4	10.5 ± 0.4	10.9 ± 0.3
DSFG	11.0 ± 0.1	11.0 ± 0.1	10.5 ± 0.1	8.3 ± 0.4	10.3 ± 0.4	10.5 ± 0.3

Note. Columns: (1) Component; (2) Uncorrected dynamical mass ($M_{\rm dyn}^{\rm uncorr} = M_{\rm dyn} \times \sin^2({\rm i})$); (3) Dynamical mass ($M_{\rm dyn}$) estimated using Equation 4.1; (4) Dispersion mass ($M_{\rm disp}$) estimated using Equation 4.2; (5) Dust mass ($M_{\rm dust}$) estimated using Equation 4.3; (6) Gas mass derived from dust mass and a gas-to-dust ratio (GDR) ($M_{\rm gas}$); (7) Molecular gas mass derived from [CII] luminosity using Equation 4.4 from Zanella et al. (2018) ($M_{\rm mol}$). All masses are reported in $M_\odot$.

κ_d at 850 μm is 0.077 m^2 kg^{-1}, then κ_d can be calculated as $\kappa_d = 0.077 \times (850/\lambda_{\rm rest})^\beta$ m^2 kg^{-1}. We use $T_d = 45 \pm 5$ K and $\beta = 1.6 \pm 0.5$, same values used for the SEDs estimations. We need to be aware that since SFRs and $M_{\rm dust}$ are estimated from the same measurements of continuum emission, both quantities are correlated.

The estimated $M_{\rm dust}$ are in Table 4.1. For the QSO host $M_{\rm dust} \sim 10^{8.5\pm0.4}$ $M_\odot$ which is consistent with the result reported by N20. For the DSFG, the dust mass is $\sim 10^{8.3\pm0.4}$ $M_\odot$, which is higher than the $M_{\rm dust}$ estimations in N20. This discrepancy in the DSFG is mainly due to the higher continuum emission measured with Cycle 6 data. The uncertainties in the dust masses include the errors in the measurements of the continuum emission and the errors based on the literature for the dust temperature and the dust emissivity coefficient β. The uncertainties were then set to $\Delta T = 5$ K (Sommovigo et al., 2022) and $\Delta\beta = 0.5$ (e.g., da Cunha et al., 2021; Algera et al., 2023). The contribution of the errors in the continuum emission and T_d have a small impact compared to the uncertainties from β.

4.3. Gas masses $M_{\rm gas}$

Molecular gas (H_2) is the most abundant molecule in the ISM but is difficult to detect in emission due to its lack of a permanent dipole moment and the high temperatures necessary to excite the rotational transitions, which mean that direct observations of H_2 can only trace a small and warm (T > 100 K) fraction of the total molecular gas. For this reason, other molecules have been used as tracers of cold H_2 with the most common one being CO, as well as the FIR/sub-mm dust continuum, and recently, [CII].

In this context, we determine the gas masses of our galaxies following two different methods. In the first one, we calculate the total $M_{\rm gas}$ (atomic + molecular) using the dust mass $M_{\rm dust}$ obtained from the FIR continuum emission (see Magdis et al., 2012; Santini et al., 2014; Genzel et al., 2015; Scoville et al., 2017) with a gas-to-dust ratio (GDR) of 100 as used in N20, based on the Draine et al. (2007) determination of GDR for local, solar metallicity galaxies. The gas-to-dust ratio can vary significantly among high-z galaxies, with studies showing a wide range of values (Ivison et al., 2010 with a GDR $\sim$ 40 at $z = 2.3$, Banerji et al., 2016 finding a GDR $\sim$ 30 - 110 at $z \sim 2.5$). These lower ratios are unexpected as the

GDR scales inversely with metallicity (Leroy et al., 2011; Rémy-Ruyer et al., 2014) and high-z sources are known to have lower metallicities than local galaxies. This discrepancy can be a result of the methodology used in those works to determine the GDR values as it is based on dust measurements and gas masses estimated from the CO line, which requires choosing a value for the CO-to-H_2 conversion factor (α_{CO}), a parameter that is highly dependant on the properties of the galaxy, including its metallicity both in local faint galaxies (Leroy et al., 2011) as well as high-z galaxies (Heintz et al., 2021; Sanders et al., 2023). Because of this, we prefer to continue using a GDR of 100, but it has to be noticed that our mass estimates will scale with any new revised values of this adopted ratio.

The estimated gas mass for our sources is $M_{\rm gas} \sim 10^{10.5\pm0.4}\ M_\odot$ for the QSO host and $\sim 10^{10.3\pm0.4}\ M_\odot$ for the DSFG. The uncertainties in the gas masses are based on the errors in the dust masses estimations only and therefore they are expected to be larger if we include the uncertainties from the fixed value of the GDR.

The other methodology is based on the correlation between [CII] luminosity and the molecular gas mass in galaxies. Several works have discussed the reliability of the [CII] λ157.74 μm to trace the molecular gas in galaxies with different physical properties (Madden et al., 2020; Dessauges-Zavadsky et al., 2020; Vizgan et al., 2022). Particularly, at high-z the determination of the molecular gas content becomes challenging. As the metallicity of the galaxies decreases with redshift, common tracers such as CO and dust are not as efficient as they are in the local universe because the dust abundance decreases and the CO molecule is dissociated and ionized into C and C^+ but H_2 molecule is either dust or self-shielded from UV radiation leading to a fraction of H_2 that is not being traced by carbon monoxide (CO-dark).

Recently, Zanella et al. (2018) (hereafter Z18) have probed that the [CII] line is a convenient tracer of molecular gas content regardless of the galaxy nature, from a normal main-sequence (MS) galaxy to a starburst galaxy, including metal-poor galaxies. Using a sample covering a redshift range of $0 < z < 6$ and metallicities $7.9 < 12 + \log({\rm O/H}) < 8.8$ they found that [CII] luminosity ($L_{\rm CII}$) correlates with the molecular gas mass ($M_{\rm mol}$) in a linear relation following Equation 4.4:

$$\log L_{\rm CII} = -1.28(\pm0.21) + 0.98(\pm0.02) \log M_{\rm mol} \tag{4.4}$$

with a dispersion of 0.3 dex and a Pearson coefficient $\rho = 0.97$, suggesting a statistically significant correlation between these two parameters. Nonetheless, the Z18 relation is derived from different samples of galaxies in the literature with measurements of [CII] and molecular gas masses estimated from CO or dust continuum. These quantities were not calibrated to account for the fraction of molecular gas at high-z that is not traced by CO molecule ("CO dark" gas) or by dust in lower metallicity galaxies.

From this relation, they constrained the $L_{\rm [CII]}$-to-H_2 conversion factor using Equation 4.5.

$$\alpha_{\rm CII} = L_{\rm CII}/M_{\rm mol} \tag{4.5}$$

They estimate an $\alpha_{\rm CII} = 30\ M_\odot/L_\odot$ for the sample of main-sequence and starburst galaxies, which led them to propose that $\alpha_{\rm CII}$ is unique and independent of the source mode of star formation, as well as it is largely independent of the galaxy depletion time, metallicity, and redshift. However, Vizgan et al. (2022) simulations of high-z galaxies suggested an $\alpha_{\rm CII}$ factor that has indeed a weak dependency on metallicity, especially if extremely metal-poor systems are included.

Using the Z18 relation we estimate a molecular gas mass of $M_{\rm mol} \sim 10^{10.9\pm0.3}\ M_\odot$ for the QSO host and $M_{\rm mol} \sim 10^{10.5\pm0.3}\ M_\odot$ for the DSFG, with uncertainties similar to the dispersion reported by the Z18 fit, which suggests that our errors are mainly dominated by the relation itself than by the uncertainties in $L_{\rm CII}$. Both masses are larger than those determined using the dust continuum and a GDR= 100.

4.4. Schmidt-Kennicutt relation

To understand galaxy evolution, we require a complete characterization of the star formation rate and the processes in the ISM that triggers it. The most common parametrization to connect the SFR with the total (atomic + molecular) gas mass is a power law introduced by Schmidt (1959) and Schmidt (1963) which is usually expressed in terms of surface densities:

$$\Sigma_{\rm SFR} = A(\Sigma_{\rm gas})^n \tag{4.6}$$

with A the star formation efficiency. For this parametrization, Kennicutt (1998) (K98 hereafter) found a slope n = 1.4 ± 0.15 for a sample of local galaxies that included 61 normal star-forming galaxies and 36 infrared-selected starburst galaxies. This correlation has been probed to be thigh along several orders of magnitudes for both, the star formation surface density ($\Sigma_{\rm SFR}$) and the gas surface density ($\Sigma_{\rm gas}$). Since then, several publications have reexamined the results in K98 using more extensive samples of different types of galaxies including dwarf galaxies (e.g., Bigiel et al., 2008; Leroy et al., 2008; de los Reyes & Kennicutt, 2019).

In this thesis, we will take the molecular gas version of the Schmidt-Kennicutt (SK) relation in K98 and the SK relation for high-z sources of Swinbank et al. (2012) to estimate the SFRs based on the molecular gas masses obtained from the [CII] luminosities using Z18 (Section 4.3). We will compare these predictions to our estimations of the SFRs derived in Section 3.2.1 using the FIR luminosities obtained by integrating the SEDs constructed using T = 45 K and $\beta = 1.6$. Nonetheless, caution should be taken when considering the results for the SFR of the QSO host using the SK relations, which are not fitted for AGN hosts and therefore they are not taking into account the presence of this central source. There is still not a complete understanding of the effects of the AGN in the interstellar medium of the galaxy but it is expected that the AGN radiation ionizes the gas from the central region, inhibiting the SF. However, the spatial and time scale of the AGN influence is still in debate.

The coefficients for the molecular SK relation in K98 were estimated using only the starburst subsample. The value for the slope of the relation is n = 1.4 and the star formation efficiency (A) is 2.1×10^{-4} $M_\odot$ yr^{-1} kpc^{-2} (see Figure 5 of K98). Using this relation we find for the QSO host, a SFR of approximately $(2.14 \pm 2.01) \times 10^2$ $M_\odot$ yr^{-1}. In the case of the DSFG, the SFR is $\sim (0.58 \pm 0.55) \times 10^2$ $M_\odot$ yr^{-1}.

In Swinbank et al. (2012) the best fit parameters of the SK relation were obtained using a sample of nine star-forming galaxies at $z = 0.84$–2.23 selected from the UKIRT/HiZELS survey. The best fit for the slope was n = 1.34 ± 0.15 with A = 3.4×10^{-4} $M_\odot$ yr^{-1} kpc^{-2}, in line with the coefficients estimated in K98 using the local sample. For our sources, this yields a SFR = $(3.6 \pm 3.3) \times 10^2$ $M_\odot$ yr^{-1} for the QSO host and SFR = $(1.1 \pm 1) \times 10^2$ $M_\odot$ yr^{-1} for the DSFG. These results are of the same order of magnitude as the ones obtained using K98 but slightly higher, which can be expected considering that the relation is suited for high-redshift sources, which tend to exhibit higher SFRs (Madau & Dickinson, 2014), resulting also in higher values of $\Sigma_{\rm SFR}$.

To estimate the uncertainties in the SFRs using the SK relations we consider only the errors associated with $M_{\rm mol}$ obtained using Z18, as they are expected to dominate over the errors in the determination of the SK coefficients. In fact, even though the relation in Z18 holds for at least 5 orders of magnitude, the observed scatter implies that individual determinations can at best be obtained with 0.3 dex in error. Hence, the uncertainties in the SFR estimations using the SK relations with Kennicutt (1998)) and Swinbank et al. (2012) coefficients are considerably large, close to a factor ≈ 1.

In comparison, using Equation 3.1 with the FIR luminosities of our sources we estimated a SFR of $\sim 402 \pm 51$ $M_\odot$ yr^{-1} for the QSO host, which is consistent with the value obtained using K98 and Swinbank et al. (2012). For the DSFG, the SFR was $\sim 244 \pm 38$ $M_\odot$ yr^{-1}, similar to the result obtained using Swinbank et al. (2012) coefficients and still comparable to the value obtained using K98. The formal uncertainties of these SFRs are considerably smaller than the ones using $L_{\rm CII}$. However, we can still argue that the SFRs obtained with the SK relations are consistent to those obtained using the $L_{\rm FIR}$ estimates. In fact, several studies have discussed the direct connection between the $L_{\rm CII}$ and the SFR for local and high-redshift sources (e.g., De Looze et al., 2014; Herrera-Camus et al., 2015; Carniani et al., 2020; Schaerer et al., 2020), finding mixed results.

4.5. Main sequence of galaxies

The relation between the star formation rate (SFR) and the stellar mass ($M_\star$) of galaxies is known as the star-forming main sequence of the galaxies (MS). The term was first introduced by Noeske et al. (2007) for the relation at redshift $z < 1$. Observations at $z < 4$ show that the MS seems to have a constant slope, close to unity (Tomczak et al., 2016; Santini et al., 2017). However, the MS needs to be normalized to account for the increase of star formation per unit stellar mass as the redshift increases. This normalization depends on the sample selection and SFR tracer used Speagle et al. (2014). For low and high-z galaxies, a redshift-dependent turn-over mass (M_0) has been observed for stellar masses $M_\star > 10^{10.5}$ $M_\odot$

(Lee et al., 2015; Schreiber et al., 2015; Tomczak et al., 2016; Leslie et al., 2020). In this work, we study the position of our two main components in the J205724.14 system relative to the MS relation for high-z sources. We use the gas masses derived from dust and the molecular gas mass derived from the [CII] luminosity using Equation 4.4 (from Z18) to determine their stellar masses.

Assuming that the total dynamical mass is $M_{\rm dyn} = M_{\rm gas} + M_\star$ (i.e., that dark matter is not dominant within the galactic radius where the dust and gas emission have been traced) we can estimate $M_\star$ by subtracting the fraction of gas mass from the total (inclination corrected) dynamical mass of each source. We see that both of our sources have $M_{\rm gas} < M_{\rm dyn}$ which is a physically sound result, indicating that the adopted GDR is plausible for our sources. The gas masses estimated using $M_{\rm dust}$ are consistent with a gas content $M_{\rm gas} = 0.2 \times M_\star$ for the QSO host and $M_{\rm gas} = 0.25 \times M_\star$ for the DSFG. The gas content using $M_{\rm mol}$ from $L_{\rm CII}$ is $M_{\rm gas} = 0.4 \times M_\star$ for the QSO host and $M_{\rm gas} = 0.5 \times M_\star$ for the DSFG. These values are in good agreement with the $f_{\rm gas}$ found in the literature, corresponding to $\sim$ 0.5 - 0.8 and determined for non-active galaxies out to $z \sim 4$, which means that a direct determination of their stellar masses is possible as there is no AGN contamination to the near-infrared (NIR) or optical emission of these galaxies (see N20 and references therein).

Figure 4.1 shows the position of our sources adopting stellar masses derived from dust and [CII] emission, as described above. We also plot the stellar masses of the QSO host and the DSFG as estimated in N20 assuming $f_{\rm gas} = 0.6$. We call this our third stellar mass determination. We include MS relations taken from Speagle et al. (2014) based on a compilation of 25 studies of galaxies at $0.16 < z < 3.15$, after correcting the derived SFR from Kroupa IMF to a Chabrier IMF for consistency with our work. The second MS relation is the parametrization from Equation 9 of Schreiber et al. (2015) for galaxies at redshifts $4 < z < 5$, after correcting the derived SFR from a Salpeter IMF to a Chabrier IMF. The last one is the Tomczak et al. (2016) curve for galaxies at redshifts $3 < z < 4$.

The QSO host seems to be beyond the turn-over mass (M_0) of the MS reported in the literature and laying close to the MS curves from Speagle et al. (2014) and Schreiber et al. (2015) if we expand these relations to higher masses than those used in their works (Figure 4.1 dotted lines). If we compare with Tomczak et al. (2016), the QSO host seems to be above the right end of the curve ($M_\star \sim 10^{11}\ M_\odot$), which is in agreement with the findings of N20, where all FIR-Faint sources seem to be above the MS relations used for comparison (Schreiber et al., 2015; Tomczak et al., 2016). For the DSFG the three methods to estimate the $M_\star$ are in good agreement and the position of the galaxy is on or close to all the MS relations plotted, suggesting that our DSFG is likely a MS galaxy at this cosmic time. This result is robust even considering the uncertainties for $M_\star$. However, as already discussed, the uncertainties in the determinations of $M_\star$, using any of the three methods described, are expected to be larger than the formal errors reported in this section.

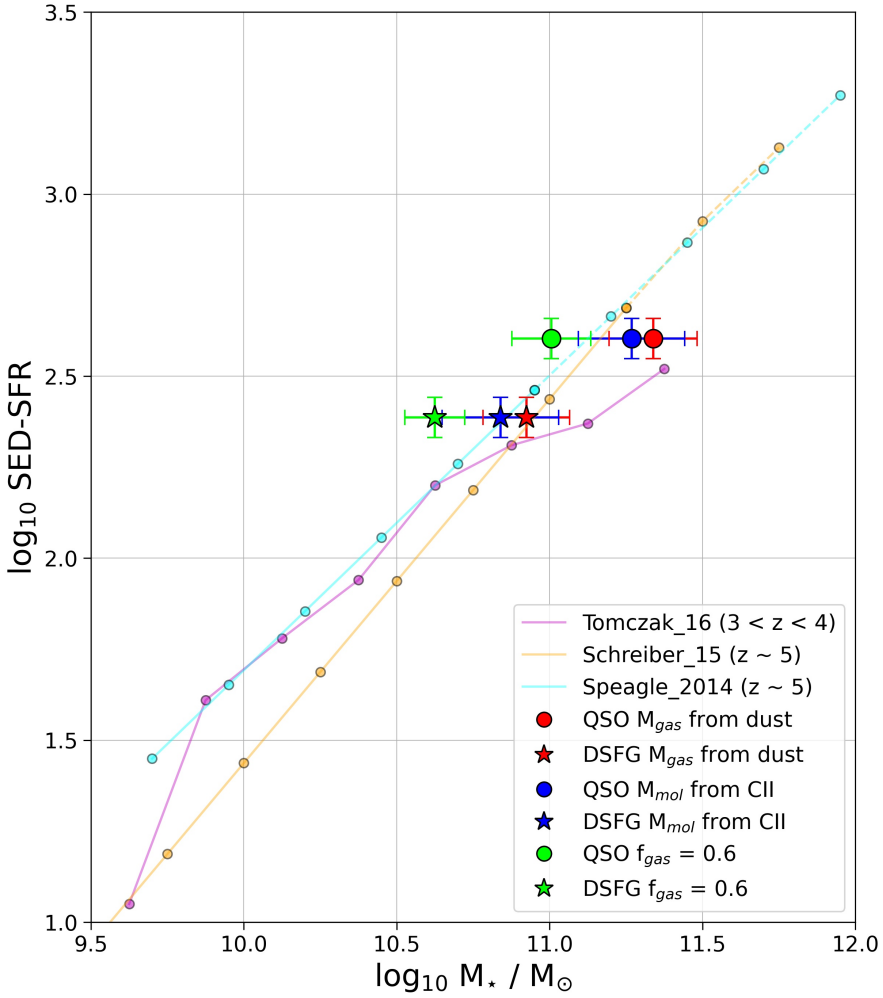

Figure 4.1: Stellar mass vs star formation rate (main sequence of star-forming galaxies). The filled circle and star represent the QSO host and the DSFG, respectively. We estimate the stellar mass using $M_\star$ = (1 - $f_{\rm gas}$) $M_{\rm dyn}$ with $f_{\rm gas} \equiv M_{\rm gas}/M_{\rm dyn}$. When $M_{\rm gas}$ is calculated using the dust mass $M_{\rm dust}$ and a gas-to-dust ratio (GDR = 100) the markers are colored red. When the $M_{\rm gas}$ comes from the curve of Zanella et al. (2018) the markers are blue. For the case $M_\star$ = 0.4 $M_{\rm dyn}$ (as done in Nguyen et al., 2020) the markers are green. For comparison, three different MS curves for high-z sources are plotted: Speagle et al. (2014) in cyan, Schreiber et al. (2015) in orange and Tomczak et al. (2016) in purple.

Chapter 5

Discussion

In N20, based on ALMA Cycle 4 observations, J205724.14 was already described as a perturbed system, with the quasar host showing strong evidence of dynamical disruption with the presence of a tidal-like structure extending in the EW direction and the presence of a dusty star-forming galaxy companion (DSFG) that showed secondary peaks in [CII] and continuum which was considered an indicator of gravitational perturbations. In this thesis, we deepen that study with ALMA Cycle 6 data, collecting all the morphological characteristics and physical properties of the sources that contribute to the discussion of the J205724.14 system representing a major merger at $z \sim 4.6$.

Looking at the new data, the [CII] observations show that the system is not only composed of the quasar host and the DSFG but instead, it is a dense environment full of gas surrounding the main two components with several smaller clumpy structures, which are mostly undetected in continuum emission. The presence of these blobs gives us a hint that we are in the presence of a strongly interactive scenario, where the sources have been perturbed due to gravitational forces. This is supported by our results, where the QSO and the DSFG are spatially separated by $\sim$ 20 kpc and kinematically close with a velocity offset of $\sim$ -68 km s^{-1}. This result is in agreement with merger systems observed at high-z (see Section 3.1) and implies that both sources are undergoing a strong gravitational interaction.

Focusing on the three closest clumps to the QSO (C1, C2, and C3), which make up the "tail" of the quasar host with a length of $\sim$ 10 kpc (see Section 2.4), we discuss two different explanations for this emission. The first one is the possibility that the tail is a cold stream accretion from the CGM/IGM. However, the evidence opposes an inflow scenario as the extended emission is detected using the [CII] line, which suggests that the tail is already metal enriched and does not represent pristine gas being accreted from the IGM/cosmic web. It also seems at odds with the theoretical expectations that cold flows should present large amounts of angular momentum, which is not supported by the observed velocity field. We also consider it unlikely to represent an outflow as the tail has a very narrow velocity range, which is in disagreement with the outflows reported in the literature (e.g., broad [CII] wings of SDSS J1148+5251 at $z \sim 6$ from Maiolino et al. (2012); Cicone et al. (2015)).

In our second hypothesis, the tail is a tidal stream from a major merger between the QSO

host and the DSFG. This kind of tidal tail is commonly observed in local merging systems (see Section 1.2 for further details), where usually one tail emanates from each galaxy involved in the interaction (e.g., NGC 4676 "The Mice"; Arp 295; M51 + NGC 5195; NGC 4038/9" The "Antennae"). However, there are also observations of single tails like ours at low-z (e.g., Arp 100, 101, 173, 174). The single tail of the J205724.14 quasar is particularly bright in [CII] with a considerable extension of a dozen kpc. Such a prominent tidal feature may represent a prograde interaction, where the disk spin is aligned with the angular momentum of the orbit as seen in simulations (Privon et al., 2013). Therefore, the absence of the counterpart tail in the companion could be explained by the DSFG having a retrograde spin or by having a dynamically warmer disk. Without proper modeling of the disk of our QSO host and DSFG and more detailed observations of the system dynamics it is not possible to test these ideas.

The undetected continuum emission of these clumps can be explained as tidal tails observed at low-z usually corresponds to material pulled out from the outer regions of the disks of galaxies, where the metallicity tends to be lower and have lower dust masses. Then, a dust-poor tail is not completely unlikely. A feature of the observed single tail is its straight geometry. This could be a projection effect, which could be the result of a curved tail seen almost edge-on, in which case there should be a velocity gradient along the tail that we cannot confirm. In fact, the spectral signatures of the three clumps closer to the quasar (C1, C2, C3) do not appear to show a systematic velocity shift, but instead complex kinematics with embedded substructures. However, from the analysis of the COSMOS field, Ren et al. (2020) found that straight tails are almost as common as curved ones, even though simulations show that they should be rare and the result of prolonged encounters (Struck & Smith, 2012). They also found that even though long tails are mostly associated with the late stages of a merger, distances of 20 kpc or more (which corresponds to the distance between the DSFG and QSO) are still present in $\sim 30\%$ of the cases.

There is another feature that we might expect in this merger: a tidal bridge connecting both galaxies which is absent in J205724.14. For this we propose that S0 and S1 are indeed "real" sources and represent such a bridge between our QSO host and its companion. If this is not correct, we could explain this missing feature as being fainter enough to be below our detection threshold or so short-lived that it has already been accreted. Hence, even if the bridge is not present, the merger scenario is still strong. Our system could correspond to a high-z analog to the systems Arp 101 or Arp 173 (see Figure 5.1 and 5.2).

Finally, we draw the attention to the presence of C4, a clump located at $\sim$ 28 kpc from the QSO and $\sim$ 42 kpc from the DSFG. The presence of this source, clearly at the same redshift as the rest of the system, shows that the sources associated to J205724.14 span at least 50 kpc in size. This is comparable to WISE J224607.56-052634.9 (Díaz-Santos et al., 2018). However, while WISE J224607.56-052634.9 corresponds to one of the most luminous sources known in the IR, our system corresponds was originally classified as FIR-faint. In fact, the SFR of the main sources and other substructures are found to be rather modest in a range from 38 to 402 $M_\odot$ yr^{-1}, and they are found close or on the MS of star-forming galaxies with stellar masses $\log(M_\star) \sim 10^{11.2\pm0.1}$ $M_\odot$ for the QSO host and $\sim 10^{10.8\pm0.1}$ $M_\odot$ for the DSFG.

Finally, the merger state of the J205724.14 system and the QSO host SF activity plus the ac-

creting SMBH luminosity $L_{\rm bol} \sim 10^{47.36}$ erg s^{-1} are inconsistent with the evolutionary model for quasars proposed by Sanders et al. (1988). In this model, obscured quasars (type II) are mainly fueled by major mergers between gas-rich galaxies that cause episodes of rapid starburst and SMBH growth. During this phase, most of the accretion onto the central regions of the galaxies is expected to occur while the SMBH is enshrouded by gas and dust (Hopkins & Beacom, 2006). This would imply that most of the observed SMBHs involved in a close interaction would be severely obscured, with column densities of $N_H \geq 10^{23}$ cm^{-2} (Ricci et al., 2017). This is supported by the enhanced fraction of IR-selected AGNs compared to optically-selected AGNs in mergers (Satyapal et al., 2014). After this intense period of starburst and AGN activity, the molecular gas is expected to be expelled from the galaxy by the stellar or quasar feedback, causing a significant decrease in the SFRs and cleaning the dust from the surroundings of the SMBH. This leads to an unobscured phase for the quasar after the merging ends (Treister et al., 2010). However, J205724.14 QSO was selected in Trakhtenbrot et al. (2011) for being one of the brightest unobscured quasars at z $\sim$ 4.6 with an extremely high accretion rate $L/L_{\rm Edd} \sim 0.89$. Then following the hypothesis of Sanders et al. (1988) our system should be experiencing a low SFR caused by the final stage of the merger. Instead, we see an unobscured quasar with low SFR while the merger is not only still ongoing, but it is in the early stages of evolution. These results would imply that our understanding of the evolution of quasars is not complete and the model proposed by Sanders et al. (1988) might be too simplistic to cover all the states and processes involved in the growth of black holes in the center of galaxies.

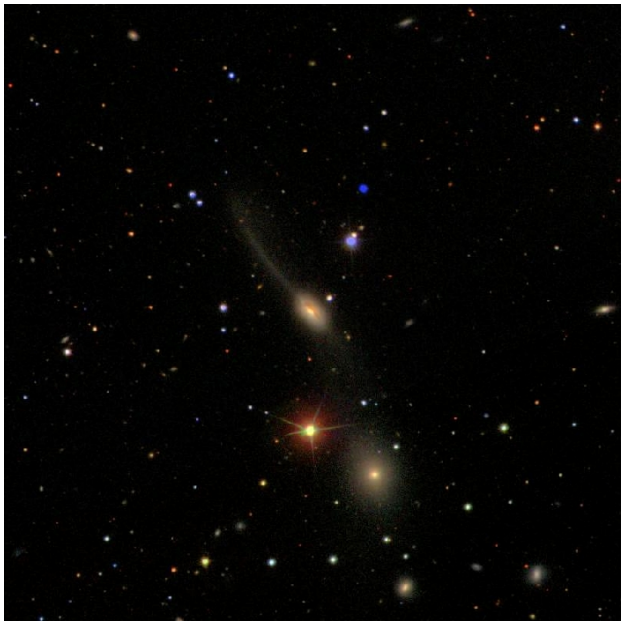

Figure 5.1: Arp 101. The spiral galaxy at the center of the image is UGC10169. The companion galaxy below is UGC 10164, an elliptical galaxy. A faint star stream bridge connects these galaxies and a long tidal star stream is visible extending out from the spiral galaxy.

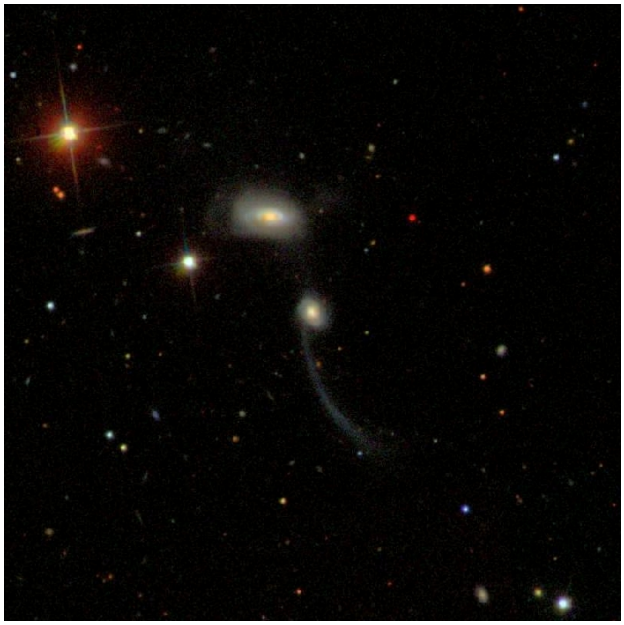

Figure 5.2: Arp 173. The larger spiral galaxy at the center of the image is MCG+02-38-020. The smaller spiral galaxy below is UGC 9561. A faint star stream bridge connects these galaxies. From the larger galaxy, a short star stream extends up and to the right. The most important feature is the narrow star stream which extends down from the smaller galaxy.

Chapter 6

Conclusion

Throughout this thesis, we have presented the results of ALMA Cycle 6 data analysis for the J2057.14 system composed of a quasar at redshift $z \sim 4.6$ and a companion dusty star-forming galaxy (DSFG), including the circumgalactic medium of these sources. The observations include the FIR emission line [CII], which arises from the ISM of the galaxies and underlying FIR continuum emission that traces the dust heated by the SF activity.

We found that the system is composed of the QSO, the DSFG and the extended [CII] emission described as a "tail" by N20 with the difference that in our work this feature is observed to be formed by three different clumps: C1, C2, and C3. Another two blobs of [CII] are discovered closer to the DSFG (S0 and S1) and a final distant clump in the SW direction of the QSO host (C4) is also observed. The QSO host and the DSFG are detected in [CII] as well as in continuum emission meanwhile all the clumps remain undetected in FIR continuum. The morphology of the DSFG as seen in the continuum is considerably more extended than it is in [CII].

The [CII] 1D spectra revealed that the QSO host and the DSFG are kinematically close, with a velocity offset of only -68 km s^{-1}, which added to the spatial separation of ~ 20 kpc, represent a strong indication that both sources are gravitationally bounded. These values are comparable to other interacting galaxies observed at similar redshift, leading us to propose that the J2057.14 system is probably undergoing a merger event. The brightness and extent of the [CII] emission suggests that we are observing a rather young event, probably after the first passage, although a more detailed characterization cannot be obtained with the current data.

We estimated a [CII]-based redshift for the QSO of $z \sim 4.683$ which is in agreement with the determination done in N20. This value is not compatible with the SDSS-based redshift of $z_{SDSS} \sim 4.663$. These differences can arise from the high uncertainties in the determination of the redshift using the last methodology as discussed in Section 3.1.1.

Using a modified black-body model we constructed the SEDs for our sources assuming T = 45 K and $\beta = 1.6$ which yield FIR luminosities of $L_{\rm FIR} \sim 10^{12.56\pm0.1}\ L_\odot$ for the QSO host and $L_{\rm FIR} \sim 10^{12.35\pm0.1}\ L_\odot$ for the DSFG. Assuming a Chabrier IMF Chabrier (2003), we estimated SFRs of $\sim 402 \pm 51$ for the QSO host and $244 \pm 38\ M_\odot\ {\rm yr}^{-1}$ for the DSFG.

We calculated the ratio between [CII] and FIR luminosity for the two main sources while reporting the lower limits for the clumps. In Figure 3.8, we observed that the quasar and DSFG are [CII] deficient and appear displaced further to higher FIR luminosities and lower values of $L_{\rm CII}/L_{\rm FIR}$, in agreement with higher redshift sources and with deficits comparable to normal SF galaxies at high-z. On the other hand, the clumps are consistent with values determined from local (U)LIRGs reported in the literature.

We estimated rough values for the dynamical, dust and gas masses of our sources (Table 4.1). The stellar masses are estimated to be $\sim 10^{11.2\pm0.1}$ and $10^{10.8\pm0.1}$ $M_{\odot}$ which locate the QSO host and the DSFG on the main sequence of star-forming galaxies when compared to high-z MS curves (Figure 4.1). This result is intriguing considering that J205724.14 unobscured QSO was selected for its brightness but its galaxy host seems to be a modest SF galaxy. Following Sanders et al. (1988) model for the evolution of quasars, for our QSO to show such characteristics, it should be in a remnant phase after the major merger has ended. In this state, the quasar would have already become unobscured and would have quenched the SFR through outflows from the stellar or BH feedback. However, the evidence of the extended gas emission surrounding the main components and especially the presence of the bright tidal tail suggest that the merger between the QSO and the DSFG has not finished and it is found somewhere after the first pericenter and the latest stage of merging.

Based on these results, we consider our system to be the perfect candidate for deeper observations using ALMA and JWST which would allow us to resolve the QSO host and DSFG and have a proper measurement of their properties (e.g., stellar mass, kinematics, circumnuclear region). Moreover, with deeper data available we could be able to model the disk of our galaxies and compare the morphology and physical properties seen in their interaction with simulations of mergers at high-redshift. Finally, comparing this system to other similar sources it will be possible to explore the complexity of the interplay between galaxies and AGN when the Universe was only a fraction of its current age.

Bibliography

Adelman-McCarthy, J. K., Agüeros, M. A., Allam, S. S., et al. 2008, The Astrophysical Journal Supplement Series, 175, 297, doi: 10.1086/524984

Alexander, D. M., & Hickox, R. C. 2012, , 56, 93, doi: 10.1016/j.newar.2011.11.003

Algera, H., Inami, H., Sommovigo, L., et al. 2023, Cold Dust and Low [OIII]/[CII] Ratios: an Evolved Star-forming Population at Redshift 7, arXiv, doi: 10.48550/ARXIV.2301.09659

Bañados, E., Venemans, B. P., Mazzucchelli, C., et al. 2018, , 553, 473, doi: 10.1038/nature25180

Banerji, M., Carilli, C. L., Jones, G., et al. 2016, Monthly Notices of the Royal Astronomical Society, 465, 4390, doi: 10.1093/mnras/stw3019

Banerji, M., Jones, G. C., Carniani, S., DeGraf, C., & Wagg, J. 2021, , 503, 5583, doi: 10.1093/mnras/stab852

Barnes, J. E., & Hibbard, J. E. 2009, , 137, 3071, doi: 10.1088/0004-6256/137/2/3071

Beelen, A., Cox, P., Benford, D. J., et al. 2006, The Astrophysical Journal, 642, 694, doi: 10.1086/500636

Bigiel, F., Leroy, A., Walter, F., et al. 2008, , 136, 2846, doi: 10.1088/0004-6256/136/6/2846

Bouché, N., Finley, H., Schroetter, I., et al. 2016, , 820, 121, doi: 10.3847/0004-637X/820/2/121

Bournaud, F., Chapon, D., Teyssier, R., et al. 2011, The Astrophysical Journal, 730, 4, doi: 10.1088/0004-637X/730/1/4

Bower, R. G., Benson, A. J., Malbon, R., et al. 2006, , 370, 645, doi: 10.1111/j.1365-2966.2006.10519.x

Carniani, S., Ferrara, A., Maiolino, R., et al. 2020, Monthly Notices of the Royal Astronomical Society, 499, 5136, doi: 10.1093/mnras/staa3178

Casey, C. M., Narayanan, D., & Cooray, A. 2014, Physics Reports, 541, 45, doi: 10.1016/j.physrep.2014.02.009

Chabrier, G. 2003, , 115, 763, doi: 10.1086/376392

Chary, R., & Elbaz, D. 2001, The Astrophysical Journal, 556, 562, doi: 10.1086/321609

Cicone, C., Maiolino, R., Gallerani, S., et al. 2015, , 574, A14, doi: 10.1051/0004-6361/20142498010.48550/arXiv.1409.4418

Cooksy, A. L., Saykally, R. J., Brown, J. M., & Evenson, K. M. 1986, , 309, 828, doi: 10.1086/164651

Czekala, I., Loomis, R. A., Teague, R., et al. 2021, The Astrophysical Journal Supplement Series, 257, 2, doi: 10.3847/1538-4365/ac1430

da Cunha, E., Hodge, J. A., Casey, C. M., et al. 2021, The Astrophysical Journal, 919, 30, doi: 10.3847/1538-4357/ac0ae0

Darvish, B., Scoville, N. Z., Martin, C., et al. 2018, , 860, 111, doi: 10.3847/1538-4357/aac836

De Looze, I., Cormier, D., Lebouteiller, V., et al. 2014, , 568, A62, doi: 10.1051/0004-6361/201322489

de los Reyes, M. A. C., & Kennicutt, R. C. 2019, The Astrophysical Journal, 872, 16, doi: 10.3847/1538-4357/aafa82

Decarli, R., Walter, F., Venemans, B. P., et al. 2018, , 854, 97, doi: 10.3847/1538-4357/aaa5aa

Decarli, R., Dotti, M., Bañados, E., et al. 2019, , 880, 157, doi: 10.3847/1538-4357/ab297f

Dekel, A., Birnboim, Y., Engel, G., et al. 2009, , 457, 451, doi: 10.1038/nature07648

Dessauges-Zavadsky, M., Zamojski, M., Rujopakarn, W., et al. 2017, Astronomy &amp Astrophysics, 605, A81, doi: 10.1051/0004-6361/201628513

Dessauges-Zavadsky, M., Ginolfi, M., Pozzi, F., et al. 2020, , 643, A5, doi: 10.1051/0004-6361/202038231

Díaz-Santos, T., Armus, L., Charmandaris, V., et al. 2013, , 774, 68, doi: 10.1088/0004-637X/774/1/68

Díaz-Santos, T., Armus, L., Charmandaris, V., et al. 2014, , 788, L17, doi: 10.1088/2041-8205/788/1/L17

Díaz-Santos, T., Armus, L., Charmandaris, V., et al. 2017, , 846, 32, doi: 10.3847/1538-4357/aa81d7

Díaz-Santos, T., Assef, R. J., Blain, A. W., et al. 2018, Science, 362, 1034, doi: 10.1126/science.aap7605

Draine, B. T., & Li, A. 2007, , 657, 810, doi: 10.1086/511055

Draine, B. T., Dale, D. A., Bendo, G., et al. 2007, , 663, 866, doi: 10.1086/518306

Dunne, L., Eales, S., Edmunds, M., et al. 2000, , 315, 115, doi: 10.1046/j.1365-8711.2000.03386.x

Farrah, D., Lebouteiller, V., Spoon, H. W. W., et al. 2013, , 776, 38, doi: 10.1088/0004-637X/776/1/38

Fensch, J., Renaud, F., Bournaud, F., et al. 2017, , 465, 1934, doi: 10.1093/mnras/stw2920

Ferrara, A., Vallini, L., Pallottini, A., et al. 2019, Monthly Notices of the Royal Astronomical Society, 489, 1, doi: 10.1093/mnras/stz2031

Ferrarese, L., & Merritt, D. 2000, , 539, L9, doi: 10.1086/312838

Francis, L., Johnstone, D., Herczeg, G., Hunter, T. R., & Harsono, D. 2020, The Astronomical Journal, 160, 270, doi: 10.3847/1538-3881/abbe1a

Fujimoto, S., Ouchi, M., Ferrara, A., et al. 2019, The Astrophysical Journal, 887, 107, doi: 10.3847/1538-4357/ab480f

Gebhardt, K., Bender, R., Bower, G., et al. 2000, , 539, L13, doi: 10.1086/312840

Genzel, R., Tacconi, L. J., Gracia-Carpio, J., et al. 2010, Monthly Notices of the Royal Astronomical Society, 407, 2091, doi: 10.1111/j.1365-2966.2010.16969.x

Genzel, R., Tacconi, L. J., Lutz, D., et al. 2015, , 800, 20, doi: 10.1088/0004-637X/800/1/20

Ginolfi, M., Jones, G. C., Bé thermin, M., et al. 2020, Astronomy &amp Astrophysics, 643, A7, doi: 10.1051/0004-6361/202038284

Gowardhan, A., Riechers, D., Pavesi, R., et al. 2019, The Astrophysical Journal, 875, 6, doi: 10.3847/1538-4357/ab0b3c

Graciá-Carpio, J., Sturm, E., Hailey-Dunsheath, S., et al. 2011, The Astrophysical Journal Letters, 728, L7, doi: 10.1088/2041-8205/728/1/L7

Gullberg, B., De Breuck, C., Vieira, J. D., et al. 2015, Monthly Notices of the Royal Astronomical Society, 449, 2883, doi: 10.1093/mnras/stv372

Gültekin, K., Richstone, D. O., Gebhardt, K., et al. 2009, , 698, 198, doi: 10.1088/0004-637X/698/1/198

Häring, N., & Rix, H.-W. 2004, , 604, L89, doi: 10.1086/383567

Heintz, K. E., Björnsson, G., Neeleman, M., et al. 2021, , 507, 1434, doi: 10.1093/mnras/stab2123

Herrera-Camus, R., Bolatto, A. D., Wolfire, M. G., et al. 2015, The Astrophysical Journal, 800, 1, doi: 10.1088/0004-637X/800/1/1

Hewett, P. C., & Wild, V. 2010, , 405, 2302, doi: 10.1111/j.1365-2966.2010.16648.x

Hickox, R. C., Mullaney, J. R., Alexander, D. M., et al. 2014, , 782, 9, doi: 10.1088/0004-637X/782/1/9

Hollenbach, D. J., & Tielens, A. G. G. M. 1997, Annual Review of Astronomy and Astrophysics, 35, 179, doi: 10.1146/annurev.astro.35.1.179

Hopkins, A. M., & Beacom, J. F. 2006, , 651, 142, doi: 10.1086/506610

Ivison, R. J., Swinbank, A. M., Swinyard, B., et al. 2010, , 518, L35, doi: 10.1051/0004-6361/201014548

Janssen, A. W., Christopher, N., Sturm, E., et al. 2016, , 822, 43, doi: 10.3847/0004-637X/822/1/4310.48550/arXiv.1604.00185

Jones, G. C., Bé thermin, M., Fudamoto, Y., et al. 2019, Monthly Notices of the Royal Astronomical Society: Letters, 491, L18, doi: 10.1093/mnrasl/slz154

Jorsater, S., & van Moorsel, G. A. 1995, , 110, 2037, doi: 10.1086/117668

Kabá th, P., Jones, D., & Skarka, M., eds. 2020, Reviews in Frontiers of Modern Astrophysics (Springer International Publishing), doi: 10.1007/978-3-030-38509-5

Kennicutt, Robert C., J. 1998, , 498, 541, doi: 10.1086/305588

Kereš, D., Katz, N., Weinberg, D. H., & Davé, R. 2005, , 363, 2, doi: 10.1111/j.1365-2966.2005.09451.x

Kormendy, J., & Ho, L. C. 2013, Annual Review of Astronomy and Astrophysics, 51, 511, doi: 10.1146/annurev-astro-082708-101811

Kormendy, J., & Richstone, D. 1995, , 33, 581, doi: 10.1146/annurev.aa.33.090195.003053

Lagache, G., Cousin, M., & Chatzikos, M. 2018, , 609, A130, doi: 10.1051/0004-6361/201732019

Lee, N., Sanders, D. B., Casey, C. M., et al. 2015, , 801, 80, doi: 10.1088/0004-637X/801/2/80

Leroy, A. K., Walter, F., Brinks, E., et al. 2008, , 136, 2782, doi: 10.1088/0004-6256/136/6/2782

Leroy, A. K., Bolatto, A., Gordon, K., et al. 2011, The Astrophysical Journal, 737, 12, doi: 10.1088/0004-637X/737/1/12

Leslie, S. K., Schinnerer, E., Liu, D., et al. 2020, The Astrophysical Journal, 899, 58, doi: 10.3847/1538-4357/aba044

Lutz, D., Berta, S., Contursi, A., et al. 2016, , 591, A136, doi: 10.1051/0004-6361/201527706

Madau, P., & Dickinson, M. 2014, , 52, 415, doi: 10.1146/annurev-astro-081811-125615

Madau, P., Ferguson, H. C., Dickinson, M. E., et al. 1996, , 283, 1388, doi: 10.1093/mnras/283.4.1388

Madden, S. C., Cormier, D., Hony, S., et al. 2020, Astronomy &amp Astrophysics, 643, A141, doi: 10.1051/0004-6361/202038860

Magdis, G. E., Daddi, E., Bé thermin, M., et al. 2012, The Astrophysical Journal, 760, 6, doi: 10.1088/0004-637x/760/1/6

Magdis, G. E., Rigopoulou, D., Hopwood, R., et al. 2014, The Astrophysical Journal, 796, 63, doi: 10.1088/0004-637X/796/1/63

Magnelli, B., Saintonge, A., Lutz, D., et al. 2012, Astronomy & Astrophysics, 548, A22, doi: 10.1051/0004-6361/201220074

Magorrian, J., Tremaine, S., Richstone, D., et al. 1998, , 115, 2285, doi: 10.1086/300353

Maiolino, R., Cox, P., Caselli, P., et al. 2005, , 440, L51, doi: 10.1051/0004-6361:200500165

Maiolino, R., Gallerani, S., Neri, R., et al. 2012, , 425, L66, doi: 10.1111/j.1745-3933.2012.01303.x10.48550/arXiv.1204.2904

Malhotra, S., Helou, G., Stacey, G., et al. 1997, , 491, L27, doi: 10.1086/311044

Malhotra, S., Kaufman, M. J., Hollenbach, D., et al. 2001, , 561, 766, doi: 10.1086/323046

Marconi, A., & Hunt, L. K. 2003, , 589, L21, doi: 10.1086/375804

Martin, C. L., Ho, S. H., Kacprzak, G. G., & Churchill, C. W. 2019, The Astrophysical Journal, 878, 84, doi: 10.3847/1538-4357/ab18ac

Martin, D. C., Matuszewski, M., Morrissey, P., et al. 2016, The Astrophysical Journal, 824, L5, doi: 10.3847/2041-8205/824/1/l5

McMullin, J. P., Waters, B., Schiebel, D., Young, W., & Golap, K. 2007, 376, 127

Mihos, J. C., & Hernquist, L. 1996, , 464, 641, doi: 10.1086/177353

Mocz, P., Green, A., Malacari, M., & Glazebrook, K. 2012

Mor, R., & Netzer, H. 2012, Monthly Notices of the Royal Astronomical Society, 420, 526, doi: 10.1111/j.1365-2966.2011.20060.x

Mor, R., Netzer, H., Trakhtenbrot, B., Shemmer, O., & Lira, P. 2012, The Astrophysical Journal, 749, L25, doi: 10.1088/2041-8205/749/2/l25

Netzer, H. 2009, Monthly Notices of the Royal Astronomical Society, 399, 1907, doi: 10.1111/j.1365-2966.2009.15434.x

Netzer, H., Lani, C., Nordon, R., et al. 2016, , 819, 123, doi: 10.3847/0004-637X/819/2/123

Netzer, H., Mor, R., Trakhtenbrot, B., Shemmer, O., & Lira, P. 2014, The Astrophysical Journal, 791, 34, doi: 10.1088/0004-637x/791/1/34

Nguyen, N. H., Lira, P., Trakhtenbrot, B., et al. 2020, The Astrophysical Journal, 895, 74, doi: 10.3847/1538-4357/ab8bd3

Noeske, K. G., Weiner, B. J., Faber, S. M., et al. 2007, , 660, L43, doi: 10.1086/517926

Nordon, R., Lutz, D., Genzel, R., et al. 2012, , 745, 182, doi: 10.1088/0004-637X/745/2/182

Onoue, M., Bañados, E., Mazzucchelli, C., et al. 2020, , 898, 105, doi: 10.3847/1538-4357/aba193

Prieto, J., Escala, A., Privon, G. C., & d'Etigny, J. 2021, , 508, 3672, doi: 10.1093/mnras/stab2740

Privon, G. C., Barnes, J. E., Evans, A. S., et al. 2013, , 771, 120, doi: 10.1088/0004-637X/771/2/120

Prochaska, J. X., Neeleman, M., Kanekar, N., & Rafelski, M. 2019, , 886, L35, doi: 10.3847/2041-8213/ab55eb

Rémy-Ruyer, A., Madden, S. C., Galliano, F., et al. 2014, Astronomy &amp Astrophysics, 563, A31, doi: 10.1051/0004-6361/201322803

Ren, J., Zheng, X. Z., Valls-Gabaud, D., et al. 2020, , 499, 3399, doi: 10.1093/mnras/staa2985

Renaud, F., Boily, C. M., Naab, T., & Theis, C. 2009, , 706, 67, doi: 10.1088/0004-637X/706/1/67

Ricci, C., Bauer, F. E., Treister, E., et al. 2017, , 468, 1273, doi: 10.1093/mnras/stx173

Romano, M., Cassata, P., Morselli, L., et al. 2021, Astronomy &amp Astrophysics, 653, A111, doi: 10.1051/0004-6361/202141306

Rosario, D. J., Santini, P., Lutz, D., et al. 2012, , 545, A45, doi: 10.1051/0004-6361/201219258

Sanders, D. B., Soifer, B. T., Elias, J. H., et al. 1988, , 325, 74, doi: 10.1086/165983

Sanders, R. L., Shapley, A. E., Jones, T., et al. 2023, , 942, 24, doi: 10.3847/1538-4357/aca46f

Santini, P., Maiolino, R., Magnelli, B., et al. 2014, , 562, A30, doi: 10.1051/0004-6361/201322835

Santini, P., Fontana, A., Castellano, M., et al. 2017, , 847, 76, doi: 10.3847/1538-4357/aa8874

Satyapal, S., Ellison, S. L., McAlpine, W., et al. 2014, Monthly Notices of the Royal Astronomical Society, 441, 1297, doi: 10.1093/mnras/stu650

Schaerer, D., Ginolfi, M., Bé thermin, M., et al. 2020, Astronomy &amp Astrophysics, 643, A3, doi: 10.1051/0004-6361/202037617

Schinnerer, E., Groves, B., Sargent, M. T., et al. 2016, , 833, 112, doi: 10.3847/1538-4357/833/1/112

Schmidt, M. 1959, , 129, 243, doi: 10.1086/146614

Schmidt, M. 1963, , 137, 758, doi: 10.1086/147553

Schreiber, C., Pannella, M., Elbaz, D., et al. 2015, , 575, A74, doi: 10.1051/0004-6361/201425017

Schweitzer, M., Lutz, D., Sturm, E., et al. 2006, , 649, 79, doi: 10.1086/506510

Scoville, N., Lee, N., Vanden Bout, P., et al. 2017, , 837, 150, doi: 10.3847/1538-4357/aa61a0

Shen, Y., Brandt, W. N., Richards, G. T., et al. 2016, The Astrophysical Journal, 831, 7, doi: 10.3847/0004-637x/831/1/7

Smith, J. D. T., Croxall, K., Draine, B., et al. 2017, , 834, 5, doi: 10.3847/1538-4357/834/1/5

Sommovigo, L., Ferrara, A., Pallottini, A., et al. 2022, Monthly Notices of the Royal Astronomical Society, 513, 3122, doi: 10.1093/mnras/stac302

Speagle, J. S., Steinhardt, C. L., Capak, P. L., & Silverman, J. D. 2014, , 214, 15, doi: 10.1088/0067-0049/214/2/15

Springel, V., Di Matteo, T., & Hernquist, L. 2005, , 361, 776, doi: 10.1111/j.1365-2966.2005.09238.x

Stacey, G. J., Geis, N., Genzel, R., et al. 1991, , 373, 423, doi: 10.1086/170062

Stacey, G. J., Hailey-Dunsheath, S., Ferkinhoff, C., et al. 2010, , 724, 957, doi: 10.1088/0004-637X/724/2/957

Struck, C., & Smith, B. J. 2012, Monthly Notices of the Royal Astronomical Society, 422, 2444, doi: 10.1111/j.1365-2966.2012.20798.x

Swinbank, A. M., Smail, I., Sobral, D., et al. 2012, , 760, 130, doi: 10.1088/0004-637X/760/2/130

Tomczak, A. R., Quadri, R. F., Tran, K.-V. H., et al. 2016, The Astrophysical Journal, 817, 118, doi: 10.3847/0004-637x/817/2/118

Trakhtenbrot, B., Lira, P., Netzer, H., et al. 2017, The Astrophysical Journal, 836, 8, doi: 10.3847/1538-4357/836/1/8

Trakhtenbrot, B., Netzer, H., Lira, P., & Shemmer, O. 2011, The Astrophysical Journal, 730, 7, doi: 10.1088/0004-637x/730/1/7

Treister, E., Natarajan, P., Sanders, D. B., et al. 2010, Science, 328, 600, doi: 10.1126/science.1184246

Treister, E., Schawinski, K., Urry, C. M., & Simmons, B. D. 2012, , 758, L39, doi: 10.1088/2041-8205/758/2/L39

Tremaine, S., Gebhardt, K., Bender, R., et al. 2002, , 574, 740, doi: 10.1086/341002

Tumlinson, J., Peeples, M. S., & Werk, J. K. 2017, Annual Review of Astronomy and Astrophysics, 55, 389, doi: 10.1146/annurev-astro-091916-055240

Vallini, L., Gallerani, S., Ferrara, A., Pallottini, A., & Yue, B. 2015, , 813, 36, doi: 10.1088/0004-637X/813/1/36

Van den Bergh, S. 1962, , 67, 486, doi: 10.1086/108757

Venemans, B. P., Walter, F., Zschaechner, L., et al. 2016, , 816, 37, doi: 10.3847/0004-637X/816/1/37

Vizgan, D., Greve, T. R., Olsen, K. P., et al. 2022, The Astrophysical Journal, 929, 92, doi: 10.3847/1538-4357/ac5cba

Vogelsberger, M., Genel, S., Springel, V., et al. 2014, , 444, 1518, doi: 10.1093/mnras/stu1536

Volonteri, M., Capelo, P. R., Netzer, H., et al. 2015, , 449, 1470, doi: 10.1093/mnras/stv387

Walter, F., Carilli, C., Neeleman, M., et al. 2020, The Astrophysical Journal, 902, 111, doi: 10.3847/1538-4357/abb82e

Wang, F., Yang, J., Fan, X., et al. 2021, , 907, L1, doi: 10.3847/2041-8213/abd8c6

Wang, R., Wagg, J., Carilli, C. L., et al. 2013, , 773, 44, doi: 10.1088/0004-637X/773/1/44

Willott, C. J., Bergeron, J., & Omont, A. 2015, , 801, 123, doi: 10.1088/0004-637X/801/2/123

Wolfire, M. G., McKee, C. F., Hollenbach, D., & Tielens, A. G. G. M. 2003, , 587, 278, doi: 10.1086/368016

York, D. G., Adelman, J., John E. Anderson, J., et al. 2000, The Astronomical Journal, 120, 1579, doi: 10.1086/301513

Zabl, J., Bouché, N. F., Schroetter, I., et al. 2019, , 485, 1961, doi: 10.1093/mnras/stz392

Zanella, A., Daddi, E., Magdis, G., et al. 2018, , 481, 1976, doi: 10.1093/mnras/sty2394

Annex A

Cycle 4 calibration issues

N20 analysis is based on ALMA Cycle 4 observations at a spatial resolution of 0.19″. The spectral setup consisted of two sidebands separated by about 12 GHz, each constructed of two spectral windows (SPWs) of width 1875 MHz. For each SPW, this spectral range is sampled by 128 channels with a frequency of 15.625 MHz or $\sim$ 15 km s^{-1} per channel. Two of the spectral windows were centered on the frequency corresponding to the expected peak of the [CII] line. The other two adjacent windows were placed at higher frequencies and used for continuum measurements. Each of these pairs of spectral windows overlapped by roughly 50 MHz. During ALMA data reduction a common flagging procedure was carried on, leading to the rejection of a few channels at the edge of the windows due to divergent flux values. As a result, there was a small spectral gap between pairs of windows, centered at a frequency of $\sim$ 334.55 GHz and it extends for about $\sim$ 150 MHz. The gap can be seen in Figure A.1 showing the [CII] spectrum for the QSO and DSFG using Cycle 4 data.

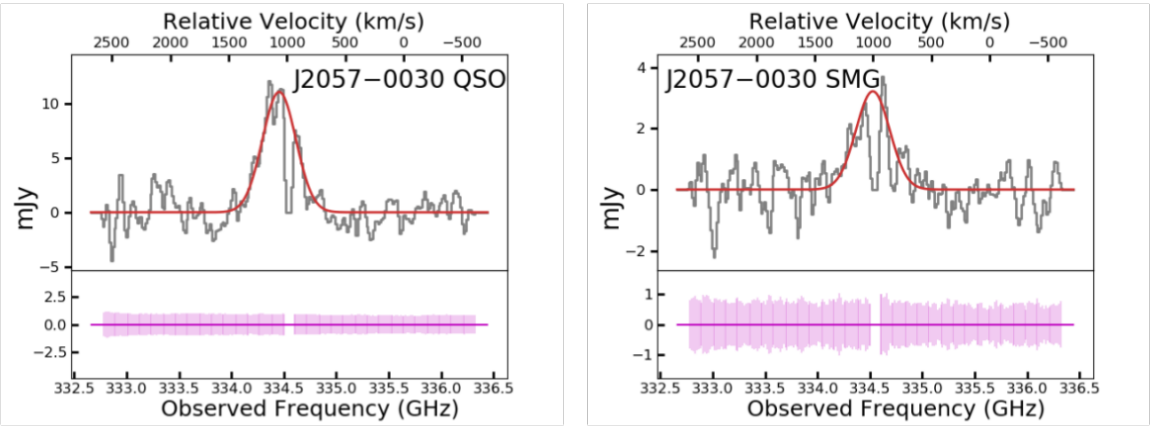

Figure A.1: [CII] spectrum of the QSO host (left) and the DSFG (right), previously identified as a sub-millimeter galaxy (SMG) in N20 (see Figure 2 of Nguyen et al., 2020). The gap is visible at a frequency of $\sim$ 334.55 GHz and it extends for about $\sim$ 150 MHz. For each spectrum, the upper x-axis denotes the velocity offsets with respect to the redshift derived from the Mg_{II} broad emission lines (Trakhtenbrot et al., 2011). Red lines show the Gaussian fits to the line profiles. RMS spectra are also included in the same scale as the flux spectrum.

Annex B

Comparison of fluxes between Cycle 4 and 6

J205724.14 system has been observed during two different cycles of ALMA. Cycle 4 was presented in N20 and Cycle 6 is presented in this work. The configurations used for each cycle are described in detail in Section 2.2. In table B.1, we summarize the main differences between them, including the number of antennae, rms, beam sizes, and pixel sizes.

For this thesis, we combined Cycle 6 observations of low and high spatial resolution (0.3″ and 0.06″, respectively) using the CASA algorithm TCLEAN. The fluxes and sizes of our sources were determined using the resulting continuum images and [CII] cubes with a beam size = 0.41″ × 0.36″. In Table B.2, we compare our measurements for the QSO host and the DSFG to the ones reported in N20. In Cycle 4, the DSFG had two different components in [CII] labeled as E and W based on their location. Two other components were detected in continuum emission and they were referred to as NE and SW. In cycle 6, the DSFG has only one component in [CII] and continuum emission.

Table B.1: ALMA observations

	N_{Ant}	F_ν rms [mJy beam^{-1}]	Beam Size [″]	Pixel Size [″]
Cycle 4[a]	39	4.4×10^{-2}	0.28 × 0.21	0.06
Cycle 6[b]	46	6.6×10^{-2}	0.42 × 0.38	0.04
	44	3.3×10^{-2}	0.11 × 0.08	0.04

Note. Columns: (1) ALMA Cycle; (2) Number of antennae; (3) Flux densities, averaging over the continuum (line-free) spectral window (in mJy beam^{-1}); (4) Beam Size (in arcseconds); (5) Pixel Size (in arcseconds).
[a] Data presented in Nguyen et al. (2020). Main issues: spectral gap between pairs of windows.
[b] New data presented in this work.

Table B.2: Cycle 4 and 6 measurements

	Comp.	Cont. Flux [mJy]	Cont. Size [″]	$F_{[CII]}$ [Jy km s^{-1}]	$FWHM_{[CII]}$ km s^{-1}	[CII] Size [″]
Cycle 4	QSO	2.03 ± 0.14	0.24×0.21	2.51 ± 0.31	331.4 ± 20.5	$0.4 \pm 0.07 \times 0.18 \pm 0.04$
	DSFG NE,E	0.28 ± 0.04	< 0.3	0.63 ± 0.11	475.4 ± 84	< 0.3
	DSFG SW,W	0.17 ± 0.06	< 0.3	0.37 ± 0.07	336.3 ± 68	0.57×0.14
Cycle 6	QSO	2.44 ± 0.24	$0.76 \pm 0.04 \times 0.68 \pm 0.03$	3.79 ± 0.39	344.9 ± 49.6	$1.14 \pm 0.05 \times 0.92 \pm 0.05$
	DSFG	1.48 ± 0.33	$1.48 \pm 0.3 \times 1.0 \pm 0.2$	1.58 ± 0.43	342.6 ± 68.8	$1.28 \pm 0.13 \times 0.34 \pm 0.03$

Note. Columns: (1) ALMA Cycle; (2) Component; (3) Continuum fluxes (in mJy); (4) Beam deconvolved sizes of the continuum emitting region (in arcseconds); (5) [CII] integrated fluxes (in Jy km s^{-1}); (6) Full width at half maximum (FWHM) of the Gaussian fit of the [CII] 1D spectra (in km s^{-1}); (7) Beam deconvolved sizes of the [CII] emitting region (in arcseconds).